TÉCNICO LISBOA

Transmit-array antenna with aberration-free scanning

Artur de Almeida Alves

Thesis to obtain the Master of Science Degree in

Electrical and Computers Engineering

Supervisors: Prof. Carlos António Cardoso Fernandes
Prof. Sérgio de Almeida Matos

Examination Committee

Chairperson: Prof. José Eduardo Charters Ribeiro da Cunha Sanguino
Supervisor: Prof. Carlos António Cardoso Fernandes
Member of the Committee: Prof. Marco Alexandre dos Santos Ribeiro

January 2021

I declare that this document is an original work of my own authorship and that it fulfills all the requirements of the Code of Conduct and Good Practices of the Universidade de Lisboa.

Acknowledgments

I would like to thank my thesis advisors Professor Carlos A. Fernandes, of Instituto Superior Técnico, and Professor Sérgio A. Matos, of Instituto Superior de Ciências do Trabalho e da Empresa, for giving me this opportunity and helping me throughout its execution, and Instituto de Telecomunicações Researcher João Felício and Laboratory Technician António Almeida for their help and prototype construction and measurements.

I also would like to thank Instituto de Telecomunicacões, UIDB/50008/2020, and project ADAM3D: PTDC/EEITEL/30323/2017, for financing all the needed material used in this thesis, and for the usage of IT laboratories, software and hardware equipment.

I thank my parents, Pedro and Paula, and my grandmother, Lúcia, for their support and patience.

I'm also thankful to the friends I made in Instituto Superior Técnico and who were by my side while I worked in this thesis, Carlos Loureiro, João Girão, Jorge Alves, Laura Mariana, Luís Rei, Pedro Bhagubai, Nuno Fernandes and Zahra Sacoor and many others who made the last years more enjoyable, both in and out of college.

Abstract

Beam steering is a vital feature of millimeter wave antennas in the context of satellite-on-the-move applications. The main challenge is to find cost-effective solutions compliant with the stringent antenna requirements of satellite communications. When compared with the electronic steering, mechanical scanning can greatly reduce the cost of the terminal. However, intrinsic aberrations of this approach need to be carefully managed. This thesis presents a new mechanical scanning design approach for Transmit-Array (TA) antennas. Usually, the TA phase correction is derived from a conversion of an incident spherical wave into a plane wave. In this work, an incoming Gaussian beam is considered instead. A Physical Optics (PO) analysis reveals that, in its ideal conditions, aberration-free scanning could be achieved. This concept is implemented by placing a thin dielectric lens in front of a horn antenna in order to produce the Gaussian illumination. Both the TA and shaping lens are manufactured using Fuse Deposition Modelling (FDM) 3D-printing in Polylactic Acid (PLA). The TA was designed for a F/D of 0.71 using dielectric unit cells with a transmission loss lower than 1.84 dB, resulting in aperture of 195 mm $\times$ 145 mm and thickness from 0.4 mm to 14.2 mm. The fabricated antenna presented a maximum gain of 27.7 dBi at 30 GHz, with a scan loss of 3.8 dB for a 51.6 degrees elevation scanning. When comparing with a traditional scanning approach with the same F/D, the proposed approach allowed a significant reduction of the overall Side Lobe Level (SLL) in the entire scanning range (SLL $<$ -16 dB).

Keywords

Ka-band, Transmit-array, beam steering, Gaussian beam

Resumo

O direccionamento de feixes é uma característica vital de antenas com comprimentos de onda nos milímetros, no contexto de aplicações satellite-on-the-move. O principal desafio é encontrar soluções de custo eficiente compatíveis com os requisitos de comunicações de satélite. Comparado com o direccionamento electrónico, o direccionamento mecânico pode reduzir bastante o custo do terminal. Contudo, aberrações intrínsicas a esta solução precisam de ser cuidadosamente geridas. Esta dissertação apresenta uma nova solução de direccionamento mecânico para antenas TA. Normalmente, a correção de fase do TA é derivada de uma conversão de uma onda esférica incidente para uma onda plana. Neste trabalho, no entanto, é considerado um feixe Gaussiano incidente. Uma análise em PO revela que, nestas condições ideais, direccionamento sem aberrações pode ser alcançado. Este conceito é implementado colocando uma lente dieléctrica fina em frente de uma corneta de maneira a produzir uma iluminação Gaussiana. Tanto o TA e a lente Gaussiana são fabricadas utilizando impressão 3D FDM em PLA. O TA foi desenhado para um F/D de 0.71 utilizando células unitárias dieléctricas como uma perda de transmissão abaixo de 1.84 dB, resultando numa abertura de 195 mm $\times$ 145 mm e uma espessura de 0.4 mm a 14.2 mm. A antena fabricada apresenta um ganho máximo de 27.7 dBi aos 30 GHz, com uma perda de varrimento de 3.8 dB para 51.6 graus de varrimento. Comparando com uma solução tradicional de varrimento com o mesmo F/D, verifica-se uma redução significativa dos SLL no alcance de varrimento total (SLL $<$ -16 dB).

Palavras Chave

Transmit-array, direccionamento de feixe, varrimento de feixe, feixe Gaussiano

Contents

List of Figures

List of Tables

Listings

Acronyms

ABS	Acrylonitrile Butadiene Styrene
CAD	Computer-aided design
CST-MWS	Computer Simulation Technology - Microwave Studio
FDM	Fuse Deposition Modelling
GL	Gaussian Lens
IT	Instituto de Telecomunicações
PO	Physical Optics
PLA	Polylactic Acid
RA	Reflect Array
SLL	Side Lobe Level
TA	Transmit-Array
VBA	Visual Basic

1

Introduction

Contents

1.1 Motivation and Objectives

Satellite communications at millimeter frequencies (30-300 GHz) provide a solution to the demand for global access to worldwide broadband internet access. For Earth to satellite connection to happen there needs to be an antenna at the ground or user terminal, which can be stationary or mobile, and another at the satellite terminal. Communications between mobile user terminals, such as terrestrial vehicles, ships and aircraft, and Geosynchronous satellites (called SOTM - Satellite on the Move), use the satellite Ka-band, more specifically 29.5-30 GHz for communications Earth to satellite, up-link, and 19.7-20.2 GHz for satellite to Earth, down-link [5]. At these high frequencies, high gain antennas need to maintain the link between the satellite and the user terminal and in the case of a mobile user terminal, the use of beam scanning or steering is necessary to direct the electromagnetic energy to the intended target and suppress it in the unwanted directions in order to avoid interference. From the multiple solutions for beam scanning, mechanical scanning is the most affordable and simplest, which is relevant for mass production, specially if made with additive manufacturing, or 3D printing, with a low cost material.

For these requirements Transmit-Array (TA) antennas are good solutions as they can be compact, lightweight and produce high gain. If produced by 3D printing they can also be very low cost and easily manufactured. A simple and low-cost strategy for beam steering can be obtained by combining a 3D printed TA with feed translation, or fixed feed with TA translation. However, as this displacement increases it results in beam aberrations which reduce the gain and thus limit the scanning performance. This dissertation proposes a new design of a TA antenna that addresses the aforementioned objectives and operates at Ka-band uplink [29.5, 30GHz]. The reduction of the beam aberrations is accomplished by making modifications to the usual concept of a TA antenna. The objective of this work is to design the proposed antenna and demonstrate by full-wave simulation and developing an experimental prototype that the concept works for the following target characteristics: directivity around 29 dBi, wide-angle steerable beam up to 50° from zenith, scan loss around 3 dB, Side Lobe Level (SLL) below -20 dB, TA in-plane dimensions of 195 $\times$ 145 mm and an F/D around 0.7.

1.2 State of the Art

1.2.1 Beam steering

With increased use of satellites for mobile broadband access applications, the need for compact, low-profile, and low-cost ground terminals increases as well.

Beam steering or scanning is the ability to steer radiation in a desired direction by changing its phase and its implementation comes mainly in the form of electronic steering [6], mechanical steering [3], or hybrid solutions [7, 8].

Electronic beam steering [6, 9–13], in the form of phased-arrays, uses multiple antenna elements to combine and direct the radiated power in the desired direction by changing the relative phases of the array elements. These antennas offer fast beam pointing, high directivity and are compact and low profile but the use of a large number of active elements increases the costs and complexity and at mm-waves, the losses in the feeding network reduce efficiency significantly.

Mechanical steering antennas are usually based on Reflect Array (RA) [14–16] or TA [3, 17–21] antennas, which are antennas composed of an array of passive phase-shifting reflective or transmitting elements, respectively, that are fed by a propagating wave, rather than a transmission line thus avoiding material losses. Each element has an associated fixed phase shift which then creates a phase distribution across the aperture of the array. These antennas are not as low profile as phased array antennas but have the advantage of needing only one primary feed, in most cases. Beam steering can be achieved by mechanical movement of either the feed or the aperture, either by horizontal translation or by translating the source along the focal arc [22]. The designing of a TA is relatively more complex than that of a RA but it has a few advantages. Because the feed is located behind the radiating aperture, it eliminates the feed blocking effect and makes the structure much more simple and easier to integrate and mount onto various platforms. This thesis focuses on the development of a TA.

1.2.2 Transmit Array Antennas

A TA antenna consists of an illuminating feed source and planar transmitting surface composed of an array of unit cells. Each cell has a different geometrical parameter that controls the transmission amplitude and phase so as to transform the incoming wave, usually spherical into a plane wave, resulting in a highly directive beam. A generic model of the TA is illustrated in Figure 1.1.

In [3] and [23] beam steering is achieved by in-plane translation of the TA in front of a stationary feed. In [3], the fabricated prototype achieved a maximum high gain of 27.3 dBi for the up-link Ka-band for the same wide-angle scan up to 50°, SLL below -10 dB and the same in-plane antenna dimensions of 195 $\times$ 145 mm, with a scan loss below 2.8 dB and an effective F/D of 0.55. In [23] the fabricated prototype achieved a gain of 15.5 dBi for for the up-link Ka-band as well, an angle scan up to 25° and scan loss of 3.4 dB for considerable smaller in-plane antenna dimensions of 80 $\times$ 80 mm.

In [24] and [25] beam steering is achieved by translation of the feed along a circular arc centered in the center of the TA. In [24] simulations achieved a maximum gain of 29.86 for the up-link Ka-band with a scan angle up to 60° and scan loss below 2.31 dB, SLL below -10 dB and in-plane antenna dimensions of 156 $\times$ 156 mm. In [25], simulations achieved a maximum gain of 25.9 dBi at 35 GHz, with SLL below -17.8 dB, angle scan up to 30° with a scan loss below 1.2 dB in-plane antenna dimensions of 69.3 $\times$ 69.3 mm. In [26] the feed also translates along a circular arc centered in the center of the TA to steer the beam but the TA is conformal instead of planar. At 25 GHz it produces a gain of 18.7 dBi, scanning

angle up to 30° and barely no scan loss, with cross section of the transmitting surface of 65 × 61.6 mm.

This thesis proposes a transmit array with a Gaussian beam feed with a corresponding lens array of unit cells such as to greatly reduce the SLL of the radiation pattern.

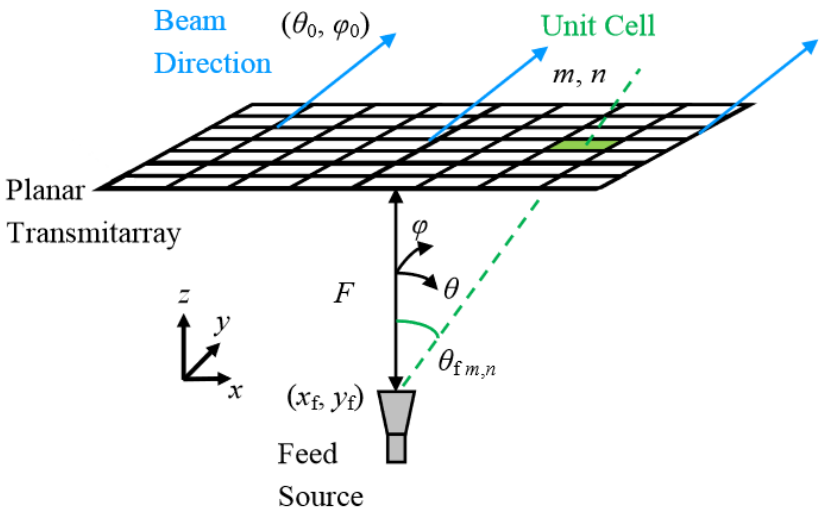

Figure 1.1: General TA antenna principle, adapted from [1].

The incident wave's phase is modified by the transmitting surface such as the phase of the outgoing wave is

$$\phi_{out} = \phi_{in} + \phi_{lens} \tag{1.1}$$

and the phase of the lens, ϕ_{lens} causes the phase correction by introducing a phase delay and different transmission coefficients so as to achieve the desired phase shift of the incident wave. This can be implemented using different techniques of unit cell design.

Usually the incident wave is a spherical wave, originating from a feed such as a horn or a patch antenna. In this thesis a different feed is proposed to attempt to eliminate the high side lobes that occur when the beam is steered away from its central position, as can be seen happening in other transmit-arrays with scanning capabilities, [3, 24–26]. Beam shaping is used in order to modify the incident wave such that its shape becomes one of a Gaussian beam and the TA lens is built accordingly.

Beam shaping is used to shape the feed into a specific type of wave or beam. Gaussian shaped beams have amplitudes whose shape is described by a Gaussian function.

Gaussian beams can be produced by a few different methods, such as using a corrugated horn as a waveguide [27] or approximated using other types of horn [28], array antenna [29], lens antenna [30] and integrated lens antenna [31].

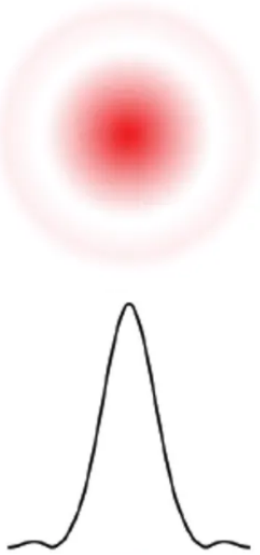

Figure 1.2: Gaussian beam intensity, adapted from [2]

1.2.3 Unit Cell Design

The design requirement for unit cells in TA antennas is to ensure that the cells produce the required phase shift, and cover the full $0 - 360^{\circ}$ range, with negligible reflection at the input side of the cell and a transmission coefficient ideally above -1 dB. A large number of phase discretization levels is recommended to diminish the effects caused by the phase transition between adjacent cells, as larger transitions lead to larger phase and reflection losses which affect the TA performance. In terms of in-plane dimensions of the cells, these are usually smaller than the wavelength being used.

The unit cell design for non-reconfigurable TA antennas can be divided into two main categories, phase delay, and phase rotation unit cells. There are many designs for phase delay unit cells as these can be constructed of different materials. Usually there is a combination of metal and dielectric materials or air gaps, in the form of layers. In [3] layers of a dielectric are intercalated with metallic square patches. In [32] the metallic layers are in the shape of cross slots and double square rings. Layers of double square rings and dieletric substract are intercalated with air gaps in [33] and with dielectric layers in [22]. In [34] an analisys is made of different cell designs. The different phase shifts are obtained by changing design parameters, such as varying the unit cells dimensions and or number of layers.

Dielectric only cells are easier and cheaper to manufacture by three-dimensional printing, also known as additive manufacturing. Dielectric printing can be done with thermoplastics, which are materials that become malleable when heated at certain temperatures and solidify upon cooling, such as Polylactic Acid (PLA) and Acrylonitrile Butadiene Styrene (ABS) [35]. These materials have a low value of relative permittivity, which implies an increase of the total thickness of the unit cells, and the lens, in order to obtain a full 360° range. Another limitation of 3D printing is the machine's precision, which puts a

constraint on the unit cells' design, specially on the case of perforated cells. Dieletric cells also have different possible designs. In [23] dielectric layers with a cross-slot element are intercalated with layers of air. Perforated dielectric only cells are used in [25], with one perforation per cell, and in [36], with four perforations per cell and where the performance of the cell with different numbers of layers is analysed. Dielectric only perforated cells are used in this thesis, as a cheap and easy solution.

Metal only cells are also used, as a solution for harsh environments such as in space, as seen in [37, 38]. It requires different machines for fabrication and is more expensive.

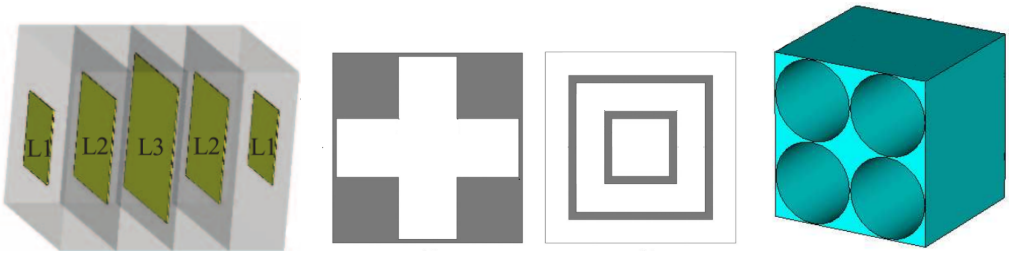

(a) Dielectric and metal square patch layers. [3].

(b) Metal cross slots and double rings layers. Adapted from [32].

(c) Dielectric only perforated cell. [39].

Figure 1.3: Examples of different types of TA cell designs.

In the case of phase rotation cells, the phase shift is achieved by the rotation of the elements of the unit cell, [40–42]. The rotation of beam can also be accomplished by simply rotating the TA.

1.2.4 Work Highlights

As is the objective of designing and fabricating a TA which eliminates aberrations created by the steering of the beam in TA antennas illuminated by a spherical wave front, this dissertation first explains the working principle of a generic TA and then that of a spherical wave feed TA and a Gaussian beam feed TA to highlight the improvements. Both theoretical results and those obtained with a Physical Optics (PO) tool combined with a Mathematica [43] script are used in these comparisons. These show a clear benefit in using a Gaussian beam feed.

To design a lens to be illuminated by the Gaussian beam, first the PLA unit cell is designed and simulated in Computer Simulation Technology - Microwave Studio (CST-MWS) [44] to obtain the behaviour of its transmission component as this will dictate how the cells need to be distributed in the lens to obtain the desired collimated plane wave. The perforated unit cell only allowed for half of the phase range, due to its size, so a second type of unit cell was added to obtain a range of almost 360 degrees and to achieve a higher overall amplitude of the transmission coefficient. Its distribution in the lens and the assembling of the lens' Computer-aided design (CAD) model is done by using Mathematica and Visual

Basic (VBA) scripts.

The lens is simulated in full wave using CST-MWS using its ideal Gaussian beam macro as the feed, producing satisfactory results. This feed cannot be produced for the prototype so a Gaussian beam feed needs to be designed. A thin PLA lens is designed in Mathematica to be used like a lens antenna, to transform the incident spherical wave front from a horn antenna into a Gaussian beam shaped output wave front. Simulations with this feed show results not very differing from those obtained with the ideal Gaussian beam. A structure is designed to be used to hold the two lenses for prototype testing and the CST-MWS simulations are repeated and contrasted to those with no structure, to observe its influence.

A TA to be illuminated by a spherical wave front is also produced and simulated with the same horn, to compare to the Gaussian beam TA.

Finally, the two TAs and the structure are printed in PLA and several measurements are taken in the anechoic chamber and compared to the simulations to see if the obtained results are as close as possible to the expected ones.

This dissertation is organized in five chapters. Chapter 1 states the objectives of the work and presents a few concepts and other relevant work developed by members of the scientific community. Chapter 2 describes the mathematical theory supporting the proposed solution. Chapter 3 describes the design of the proposed antenna and its components and the simulations showing its behaviour. Chapter 4 shows the fabricated prototype and the results of the measurements taken in the anechoic chamber and its respective results of the simulations presented in chapter 3. Chapter 5 summarizes the work done, explaining its main achievements and how the work can be continuated in the future.

2

Formulation and methods

Contents

This chapter focuses on the design of a TA lens

2.1 Working principle of a transmit-array

Figure 2.1 shows the working principle of a generic TA. The feed is located at the plane $z = 0$ and is being illuminated by a source at $(a, 0, -F)$, F being the focal distance and a being the feed translation, that is the distance from the origin $x = 0$. The output zenith angle, $\alpha(a)$ of the planar wave-front, depends on the feed translation a, which means that by translating the feed (or the lens), the output angle $\alpha(a)$ will change, thus achieving beam scanning.

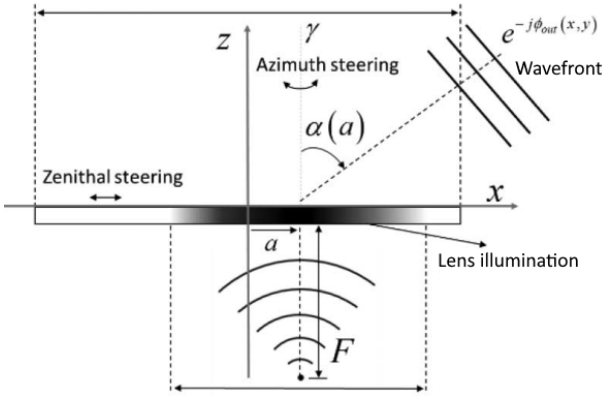

Figure 2.1: Lens working principle, adapted from [3].

To get a collimated beam the transmit-array needs to introduce a phase correction $\phi_{lens}(x, y)$, dependent on the the position on the TA and the frequency used,

$$\phi_{lens}(x, y) = -\phi_{in}(x, y)|_{a=0} + k_0 x \sin \alpha_0 \tag{2.1}$$

where $k_0 = 2\pi f/c$ is the free space wave number and $\phi_{in}(x, y)|_{a=0}$ is equal to the phase of the incident wave at the central position, which compensates the incident wave from the feed so as to obtain a collimated outgoing planar wave front and $x \sin \alpha_0$ adds an arbitrary tilt angle $\alpha(a)$, as seen in [3].

The phase of the outgoing wave is then given by the sum of the phase of the incoming wave and the phase delay imposed by the lens,

$$\phi_{out}(x, y) = \phi_{in}(x, y) - \phi_{in}(x, y)|_{a=0} + k_0 x \sin \alpha_0. \tag{2.2}$$

At $a = 0$, when the feed is in the central position, it reduces to

$$\phi_{out}(x, y)|_{a=0} = -k_0 x \sin \alpha_0, \tag{2.3}$$

which corresponds to a tilted main beam with zenith angle $\alpha(a=0)=\alpha_0$ as desired.

The dimensions of the lens are important to get the desired lens directivity. In [3] the lens directivity for a planar aperture, which represents the lens, with diameter D_A is approximated by

$$D_{max}=\eta\left(\frac{4\pi\sigma}{\lambda}\right)^2 tahn\left[\left(\frac{D_A}{4\sigma}\right)^2\right]cos\alpha_0 \tag{2.4}$$

and the minimum aperture diameter D_A by

$$D_A=\frac{1}{4\pi}\sqrt{\frac{8\tau\ln 10}{\tanh(\frac{\tau\ln\ln 10}{2})cos(\alpha_0)}\frac{D_{max}}{\eta}}, \tag{2.5}$$

where α_0 is replaced with the expression of α_a, Equation 2.21, η defines the aperture efficiency and τ corresponds to the edge field taper level $10^{-\tau}$.

This aperture diameter is also relevant for design parameter of the feed, such as the field taper, to minimize spillover. Field taper is the difference in illumination between the highest point in the center and the lowest in the edge of the aperture and. Spillover is the radiation that misses the aperture and lowers the main beam gain. These concepts are represented in Figure 2.2. Because in this case the TA is used for beam scanning by translation of the feed, the length of the lens needs to be longer than the minimum aperture diameter so it can be properly illuminated by the feed.

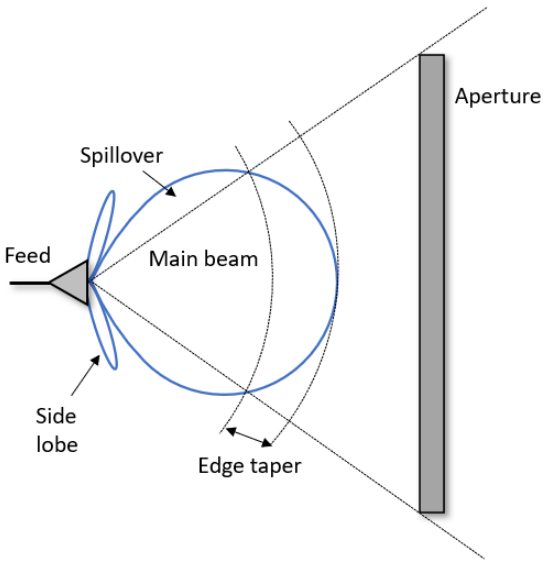

Figure 2.2: Spillover and taper concepts.

An important parameter in the minimization of beam distortion is the focal distance F, represented in Figure 2.1, which is the distance from the horn to the center of the lens. Increasing F can reduce beam distortion, SLL and scan loss due to nonlinear phase error reduction, approaching the $10log_{10}(cos\alpha_{max}/cos\alpha_0)$ limit obtained from Equation 2.4, but as antenna compactness is an issue, F

needs to be as low as possible. Scan loss is the difference in gain between the two positions with the highest and lowest gain.

To introduce the required phase delay along the lens the TA is composed of discrete phase shifting unit cells. These cells impose a spacial discretization, that is, the in plane dimensions of each cell, which are smaller than the wavelength, and a phase discretization, that is how many intervals in the $[0, 360°]$ are required. Unit cells are usually designed considering an infinite periodic structure of identical cells, in order to account for mutual coupling which happens in the actual lens. However, adjacent cells in the lens won't be equal and larger phase transitions between adjacent cells can lead to larger losses in the lens, so a large phase discretization is recommended.

2.2 Spherical source transmit-array

A typical TA fed by an incident electric field illuminating the lens has spherical phase distribution

$$\phi_{in}(x, y) = k_0\sqrt{(x-a)^2 + y^2 + F^2}. \tag{2.6}$$

Using 2.2 to express the output phase for this $\phi_{in}(x, y)$,

$$\phi_{out}(x, y) = k_0\sqrt{(x-a)^2 + y^2 + F^2} - k_0\sqrt{x^2 + y^2 + F^2} + k_0 x \sin\alpha_0 \tag{2.7}$$

In [3] Equation 2.7 is analyzed for $y = 0$, $\alpha_0 = 0$ and a feed offset of $a = -0.3F$ to better understand the factors influencing the antenna beam scanning performance.

The phase distribution exhibits a linear behavior around the point $(x = \frac{a}{2}, y = 0)$. Therefore, a first-order Taylor expansion of Equation 2.7 is performed in [3] around this point. It is expressed in Equation 2.8 as a sum of a linear term ϕ_l, which just tilts the main beam, with ϕ_{nl} representing all the remaining nonlinear terms responsible for phase aberrations.

$$\begin{cases} \phi_l(x) = \dfrac{k_0 F(a/F)^2}{\sqrt{(4 + (a/F)^2)}} + k_0\Big(\sin\alpha_0 - \dfrac{2a/F}{\sqrt{(4 + (a/F)^2)}}\Big)x \\ \phi_{nl}(x, y) = \phi_{out}(x, y) + \phi_l(x) \end{cases} \tag{2.8}$$

The output beam zenith angle $\alpha(a)$ is estimated from ϕ_l as

$$\alpha(a) = \arcsin\left[\sin\alpha_0 - \frac{2a/F}{\sqrt{(4 + (a/F)^2)}}\right], \tag{2.9}$$

which confirms that $\alpha(0) = \alpha_0$. The predicted zenith angle, or tilt, depends only on the ratio between the feed offset a and the focal distance F, which means that different values of F but the same values of

a/F the resulting tilt will be the same.

A preliminary PO analysis was done for a few a/F values to better understand these effects. The PO used was KH3D near [45], which is able to calculate the radiation pattern of an arbitrarily shaped aperture, defined by a set of node points over a grid. KH3D near evaluates the aperture near- or far-field radiation in magnitude and phase at any arbitrary distance from the specified aperture, in rectangular or spherical coordinates.

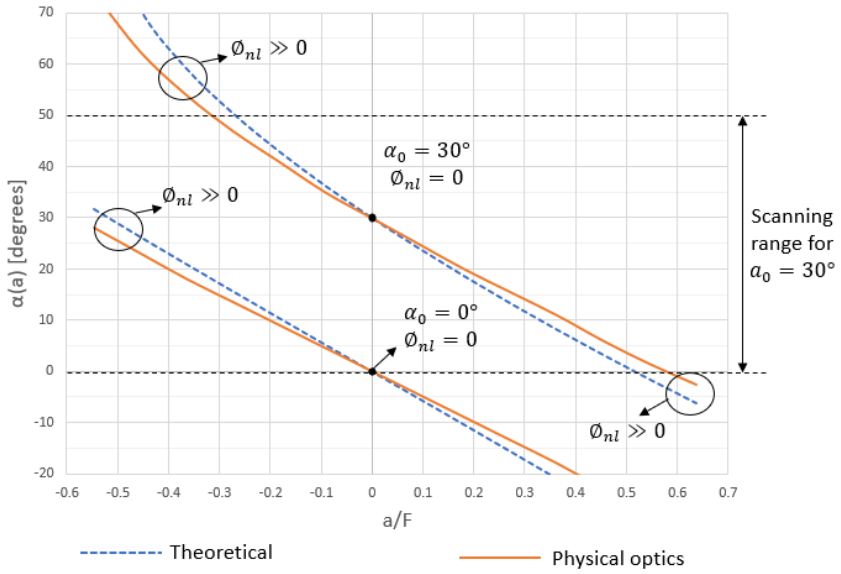

Figure 2.3: Zenith beam direction as function of the feed offset (theoretical 2.9 and PO results) for a spherical wave source.

Figure 2.3 shows an example of the the theoretical zenith beam direction given by Equation 2.9 (dashed blue curve) and the curves obtained through PO analysis which include the nonlinear phase error (solid orange curves) versus the normalized feed offset, a/F, for two different values for α_0. When $\alpha_0 \neq 0$ less displacement of the feed, a, is necessary to obtain a higher beam tilt and thus there are lower aberrations then with $\alpha_0 = 0$ as these are larger for larger displacements of the feed.

In the example of Figure 2.3, for $\alpha_0 = 30°$, the zenith scanning range $\alpha = [0, 50°]$ corresponds, according to Equation 2.9, to the feed offset $a \in [-0.25F, 0.56F]$ (see dashed blue curve in Figure 2.3.

The radiation pattern for a fixed focal distance F and varying feed translation a is represented in 2.4. The dashed black curve represents the maximum value of the radiation pattern if nonlinear phase error was zero, deduced from Equation 2.4.

The effect of the ϕ_{nl} term is noticeable for large $a/F > 0$ values. As the feed moves from the central position the effect of the nonlinear term becomes more significant as can be seen from the decay in directivity from the value which considers nonlinear phase error to be zero (dashed black curve) and from the aberrations in the main beams. This directivity decay for lower zenith angles ($a/F > 0$) is explained

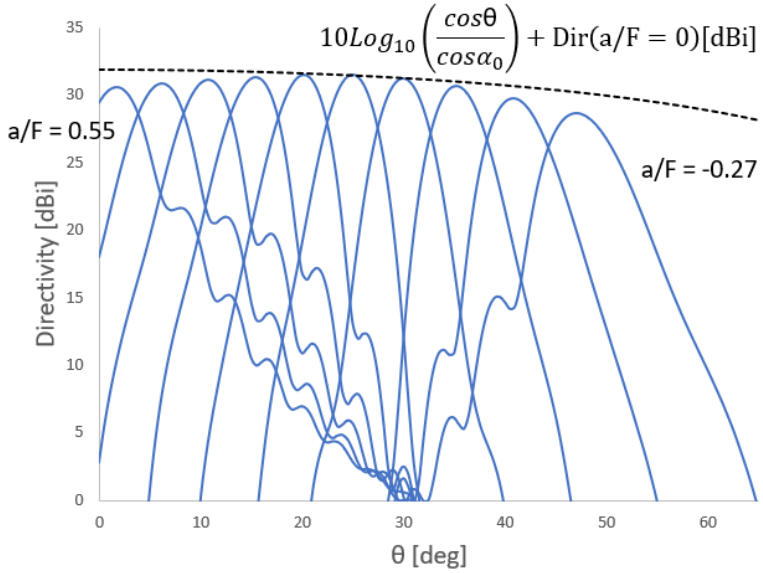

Figure 2.4: Directivity obtained by PO radiation pattern for the feed offset in the interval $a/F \in [-0.27, 0.55]$ with 0.09 steps. The dashed black curve represents the maximum normalized directivity as function of θ considering $\phi_{nl} = 0$.

by the phase error and increasing spillover, effects that counteract the increase of the effective aperture size. The directivity decay with the increase of the zenith angle, for $a/F < 0$ can be partly explained by the $cos\alpha$ reduction of the effective aperture size caused by the beam tilt. This directivity, obtained with PO, is higher than the target specification because it does not take into account effects like unit cells reflections and insertion losses, or phase errors originated by the primary feed.

To eliminate the mentioned effects of non linear phase errors, the decay in directivity and the aberrations, a different feed is proposed: a Gaussian beam. The design of a Gaussian beam source TA is studied in the next section.

2.3 Gaussian beam source transmit-array

Gaussian beams are beams of electromagnetic radiation where the electric field profile in a plane perpendicular to the beam axis can be described with a Gaussian function. The mathematical expression for the electric field amplitude of a Gaussian beam is a solution to the paraxial Helmholtz equation. Assuming polarization in the x direction and propagation in the $+z$ direction the electric field in phasor notation is given by

$$\mathbf{E}(r,z) = E_0 \frac{w_0}{w(z)} e^{\frac{-\sqrt{(x^2+y^2)}}{w(z)^2}} e^{-i(kz + k\frac{r^2}{2R(z)} - \psi(z))} \tag{2.10}$$

where $R(z)$, the radius of curvature of the beam's wavefronts at z, can be expressed as,

$$R(z) = z\left[1 + (\frac{z_r}{z})^2\right], \tag{2.11}$$

z_r, the axial distance from the beam's waist, as

$$z_r = \frac{\pi w_0^2}{\lambda}, \tag{2.12}$$

$w(z)$, the radius at which the field amplitudes fall to 1/e of their axial values at the plane z along the beam, as

$$w(z) = w_0\sqrt{1 + (\frac{z}{z_r})^2}, \tag{2.13}$$

and $\psi(z)$, the Gouy phase, as

$$w(z) = \arctan(\frac{z}{z_r}), \tag{2.14}$$

The shape of a Gaussian beam is represented in 2 dimensions in Figure 2.5.

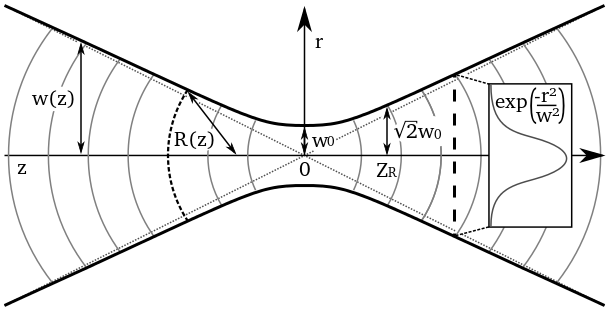

Figure 2.5: Shape of a Gaussian beam, adapted from [4].

For the case of the Gaussian beam, the expression of the wave phase at the lens input, at a distance of F is given by

$$\phi_{in}(x, y) = k_0\left[F + \frac{(x-a)^2 + y^2}{2F\left[1 + (\pi w_0^2/(\lambda F))^2\right]}\right] \tag{2.15}$$

where a is the feed offset along the x coordinate and F is the focal distance.

The phase needed to be introduced by the lens is given by

$$\phi_{lens}(x, y) = \phi_{out} - \phi_{in} = -k_0\left[F + \frac{x^2 + y^2}{2F\left[1 + (\pi w_0^2/(\lambda F))^2\right]}\right] + k_0 x \sin\alpha_0. \tag{2.16}$$

The phase of the outgoing wave is simply given by the sum of $\phi_{in}(x, y)$ and $\phi_{lens}(x, y)$,

$$\phi_{out}(x, y) = k_0\left[F + \frac{(x-a)^2 + y^2}{2F\left[1 + (\pi w_0^2/(\lambda F))^2\right]}\right] - k_0\left[F + \frac{x^2 + y^2}{2F\left[1 + (\pi w_0^2/(\lambda F))^2\right]}\right] + k_0 x \sin\alpha_0. \tag{2.17}$$

At $a = 0$ it also reduces to

$$\phi_{out}(x, y)|_{a=0} = k_0 x \sin\alpha_0. \tag{2.18}$$

Again, the function for the phase output, Equation 2.17, is analyzed for $y = 0$, $\alpha_0 = 0$ and a feed offset of $a = -0.3F$.

$$\phi_{out}(x) = -k_0[F + \frac{(x + 0.3F)^2}{2R(F)}] + k_0\left[F + \frac{x^2}{2R(F)}\right] = \frac{-k_0}{2}\frac{0.6x + 0.09F}{1 + (\frac{z_r}{F})^2} \tag{2.19}$$

The Equation 3.2 and is linear so, for a Gaussian beam feed, the output beam will not suffer distortion due to nonlinear phase error effects. But as for the spherical source wave, a first-order Taylor expansion of Equation 2.17 is performed around this point. It is expressed as a sum of a linear term ϕ_l , which just tilts the main beam, with ϕ_{nl} representing all the remaining nonlinear terms responsible for phase aberrations

$$\begin{aligned} \phi_l(x) &= \frac{k_0 F(a/F)^2}{2\big[1 + (\pi w_0^2/(\lambda F))^2\big])} - k_0\Big(\frac{a/F}{\big[1 + (\pi w_0^2/(\lambda F))^2\big]} - \sin\alpha_0)\Big)x \\ \phi_{nl}(x, y) &= \phi_{out}(x, y) + \phi_l(x) \end{aligned} \tag{2.20}$$

The output beam angle $\alpha(a)$ can be estimated from Equation 2.17 as

$$\alpha(a) = \arcsin\left[\sin\alpha_0 - \frac{a/F}{\big[1 + (\pi w_0^2/(\lambda F))^2\big]}\right] \tag{2.21}$$

and, as with a spherical feed, $\alpha(0) = \alpha_0$. Unlike in the case of a spherical wave source, the zenith angle doesn't depend only on the ratio between the feed offset a and the focal distance F, a/F, as it also depends on F alone, on the wavelength and thus the frequency, and on the beam waist, w_0, of the Gaussian beam. However, varying the value of F while keeping the same a/F will have little impact on the tilt, according to Equation 2.21, but the greater the value of F, the greater the feed displacement a will have to be to keep the same a/F and approximately the same tilt.

As for the spherical source TA, a preliminary PO analysis was done for a few a/F values to better understand these effects. Figure 2.6 shows an example of the the theoretical zenith beam direction given by Equation 2.21 (dashed blue curve) and the curves obtained through PO analysis which include the nonlinear phase error (solid orange curve) versus the normalized feed offset, a/F, for two different values for α_0. Unlike in the case of the spherical wave source, there is no noticeable effect of the ϕ_{nl} term.

In the example of Figure 2.6, for $\alpha_0 = 30°$, the zenith scanning range $\alpha = [0, 50°]$ corresponds, according to Equation 2.9, to the feed offset $a \in [-0.27F, 0.51F]$, for $F = 110$ mm, (dashed blue curve).

The radiation pattern for a fixed focal distance $F = 110$ mm and varying feed translation a is represented in Figure 2.7. The dashed black curve represents the maximum value of the radiation pattern if nonlinear phase error was zero, deduced from Equation 2.4.

In the case of the Gaussian beam source, Figure 2.7, there is no directivity decay for lower zenith

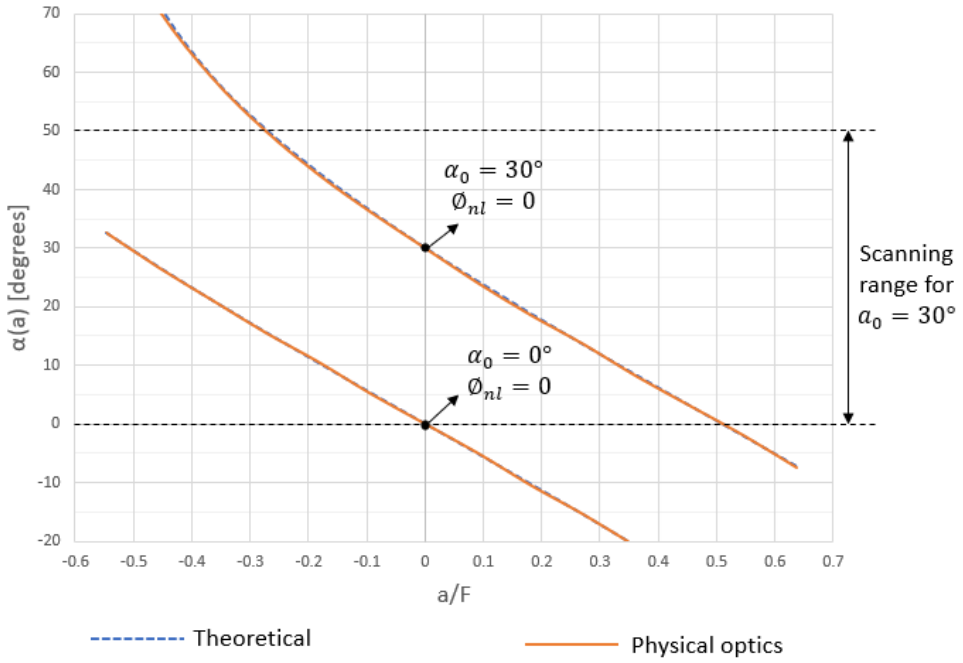

Figure 2.6: Zenith beam direction as function of the feed offset (theoretical 2.9 and PO results) for a Gaussian beam source.

angles ($a/F > 0$), as there is no noticeable nonlinear phase error, as indicated in Figure 2.6, and no aberrations in the main beams. This is why a Gaussian beam source is being proposed for a beam scanning TA.

To produce a Gaussian beam the Gaussian beam's waist position and size, z and w_0 (see Figure 2.5), have to be defined. These can be chosen considering the desired edge field taper which can be defined by the ratio of the incident field intensity at the "edge" of the lens aperture and in its center.

$$T(dB) = 20log_{10}[\frac{|E(r,z)|}{|E(0,z)|}] = 20log_{10}e^{[-\frac{r}{w(z)}]^2} \tag{2.22}$$

Solving it to $w(z)$,

$$w(z) = \frac{r}{T(dB)^{0.5}ln(10^{0.5})^{0.5}} = \frac{r}{T(dB)^{0.5}0.3393} \tag{2.23}$$

From $w(z)$, the beam waist at the central position, w_0, can be calculated from

$$w(z) = w_0\sqrt{1+(\frac{z}{z_r})^2} \Leftrightarrow w_0^4 - w(z)^2w_0^2 + \frac{F^2\lambda^2}{\pi^2} = 0 \tag{2.24}$$

Because the mathematical expression for the electric field amplitude of a Gaussian beam is a solution to the paraxial Helmholtz equation and the simulation tool used for simulations, CST-MWS, uses a

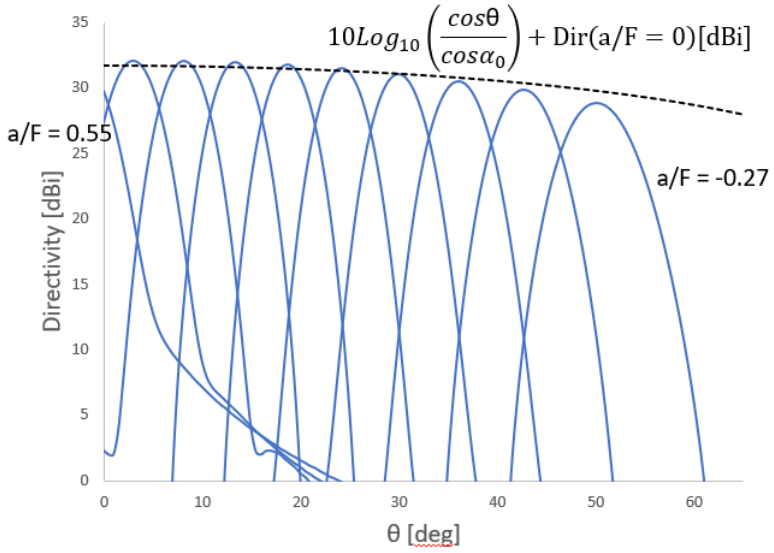

Figure 2.7: Directivity obtained by PO radiation pattern for the feed offset in the interval $a/F \in [-0.27, 0.55]$ with 0.09 step size. The dashed black curve represents the maximum normalized directivity as function of θ considering $\phi_{nl} = 0$.

paraxial approximation that assumes

$$\begin{aligned} z_r &> 4\lambda/\pi \\ w_0 &> 2\lambda/\pi, \end{aligned} \tag{2.25}$$

these conditions are applied to the choice of the value of the beam waist w_0.

CST-MWS is a 3D electromagnetic analysis software package for designing, analyzing and optimizing electromagnetic components and systems.

3

Design and Simulation Results

Contents

3.1 Gaussian beam feed

To produce a Gaussian beam feed a thin dielectric lens was designed. This lens can be 3D printed and so the feed is simple and cheap to produce. Usually dielectric lenses are designed to collimate incoming radiation into plane waves but this lens was designed so it introduces a phase delay such as to produce a Gaussian beam shaped wave. This lens will be called Gaussian lens Gaussian Lens (GL) for simplicity. The geometry of the feed and its placement in relation to the main lens is represented in Figure 3.1.

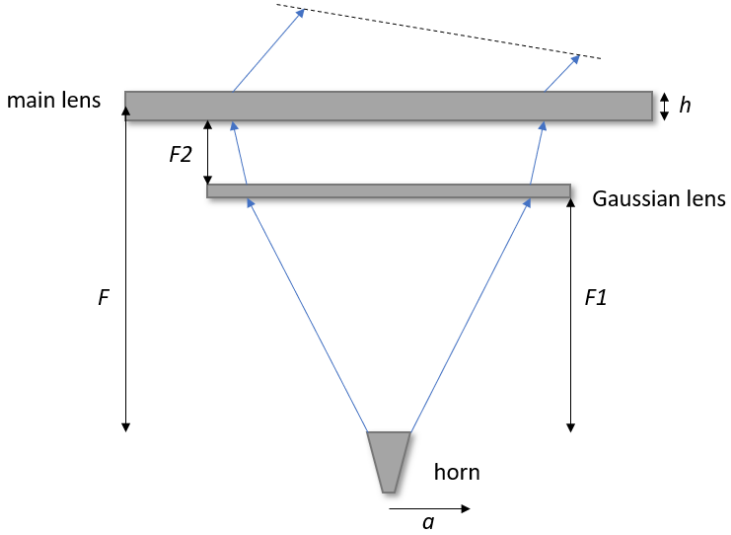

Figure 3.1: Proposed solution working principle.

The input phase is that of a spherical wave for a distance $z = F_1$,

$$\phi_{in_{sph}}(x, y) = k_0\sqrt{x^2 + y^2 + F_1^2} \tag{3.1}$$

The phase does not depend on the feed displacement a because the horn and the GL move together. The output phase is that of a Gaussian beam

$$\phi_{out_{Gauss}}(x, y) = k_0\left[F_1 + \frac{x^2 + y^2}{2F_1\left[1 + (\pi w_0^2/(\lambda F_1))^2\right]}\right]. \tag{3.2}$$

The incident and output phases are represented in Figure 3.2(a). The phase delay introduced by the lens is the difference between the phases,

$$\phi_{lens_{Gauss}}(x, y) = k_0\left[F_1 + \frac{x^2 + y^2}{2F_1\left[1 + (\pi w_0^2/(\lambda F_1))^2\right]}\right] - k_0\sqrt{x^2 + y^2 + F_1^2}. \tag{3.3}$$

To design the GL the parameters of the Gaussian beam have to be defined, based on some con-

ditions, which are a frequency of a 30 GHz, a taper of 15 dB on the surface of the main lens at $r = D_A/2 = 72.5$ mm and a focal distance $F = 110$ mm for the main lens. These conditions are used in Equations 2.23 and 2.24 and the parameters of the Gaussian beam are thus,

- $\lambda = c/f = 10$ mm
- $w_0 \approx 6.4$ mm from Equation 2.24
- $z_r \approx 12.9$ mm from Equation 2.12

Since the paraxial approximation imposes the minimum values of,

$$\begin{aligned} z_r &> 4\lambda/\pi \Leftrightarrow z_r > 12.7 \\ w_0 &> 2\lambda/\pi \Leftrightarrow w_0 > 6.4, \end{aligned} \tag{3.4}$$

$w_0 = 6.5$ mm with a $z_r = 13.3$ mm can be used to satisfy both conditions and be close to a taper of 15 dB.

The focal distance for the GL, F_1, was defined by having a fixed value for the main lens focal distance, $F = 110$ mm, and stuying the effect on the distance between the two lenses, F_2, with some PO simulations.

The focal distance for the GL, $F_1 = 30$ mm. This value was chosen so as to leave enough distance between the two lenses, F_2, to avoid having too much reflections and also enough distance from the horn to the GL, F_1 to avoid beam distortion, while keeping a fixed value for the main lens focal distance, $F = 110$ mm and the targeted directivity of 29 dBi for the central position of the feed.

The height of the dielectric GL to introduce the necessary phase shift is given by Equation 3.5 and it's represented in Figure 3.2(b).

$$\phi_{lens}(x,y) = \phi_{PLA}(x,y) + \phi_{air}(x,y) \Leftrightarrow h(x,y) = \frac{\phi_{lens}(x,y)/k_0 + h_{max}}{\sqrt{\epsilon_r} - 1} \tag{3.5}$$

where k_0 is the wave number and ϵ_r is the material's relative permittivity and $h_{max} = 20$ mm and $\phi_{lens}(x,y)$ is obtained from Equation 3.3. A constant value was added to $\phi_{lens}(x,y)$ and $h(x,y)$ in order to obtain positive values for $h(x,y)$ as is represented in Figure 3.2(b). The minimum height was set to be at least 0.27 mm to be viable for 3D printing.

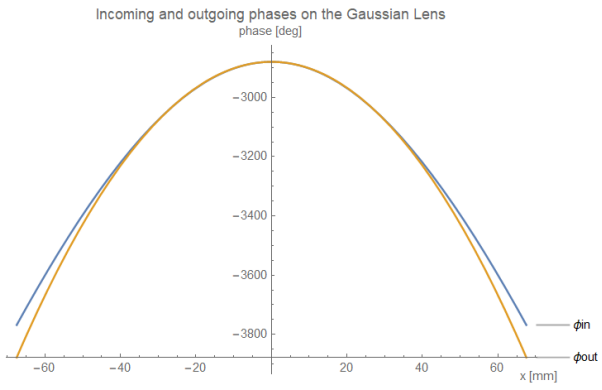

(a) Gaussian Lens's incoming and outgoing phase along the x axis.

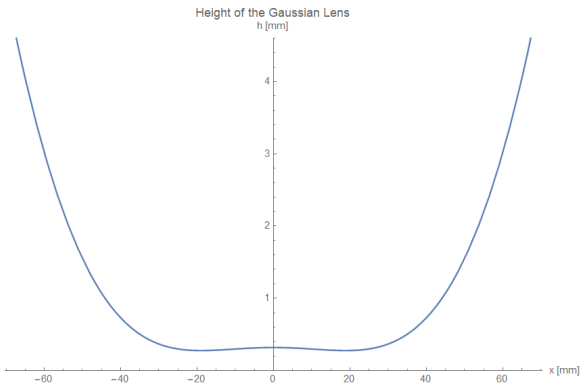

(b) Gaussian Lens's height along the x axis.

Figure 3.2: TA antenna general working principle and feed configuration.

The 3D model of the lens, shown in Figure 3.3, is made by making a 3D plot of the height, Equation 3.2(b), with a radius of 67.5 mm. This radius should be smaller than the smallest section of the main lens, $D_A/2 = 72.5$ mm and small enough so that the height does not get too high on the border where the difference in phase gets larger (see Figure 3.14) but large enough so that the incident phase in the TA lens is going through the GL and not around it. This puts a limitation on the feed displacement a, as it only enables to go so far as $a = -30$ mm and $a = 30$ mm because a higher offset would make it so part of the GL is not directly below the TA lens, which leads to high spillover.

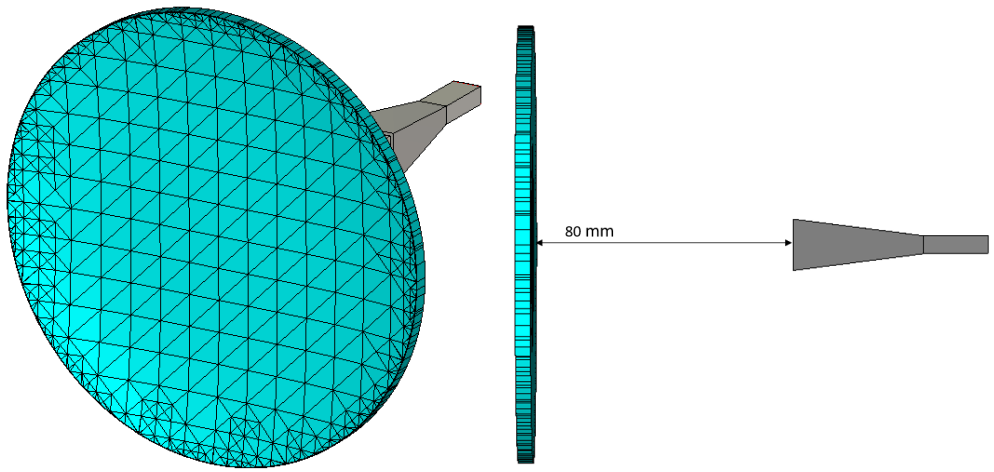

(a) 3D view.

(b) Side view.

Figure 3.3: Model of the Gaussian beam feed.

The feed composed by the GL and a horn with a gain of 14.7 dBi at 30 GHz was simulated in

CST-MWS. The resulting E-field and farfield are represented (solid blue curves) in Figures 3.4 and 3.5 respectively. Superimposed to these are the same components but for an ideal Gaussian beam produced by a CST-MWS macro (solid orange curves). The designed feed E-field of the GL and horn shows good agreement with this ideal feed, up until the borders of the GL at $x = \pm 67.5$ mm, where a larger deviation becomes visible. The radiation pattern for the farfield directivity also shows good agreement for the two feeds, with a directivity of 14.9 dBi for the GL feed and of 15.5 dBi for the CST-MWS macro at $\theta = 0°$.

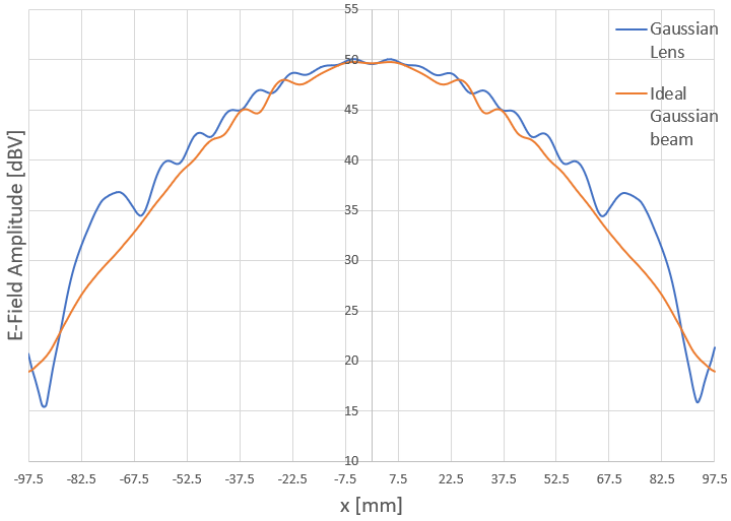

(a) Feed amplitude.

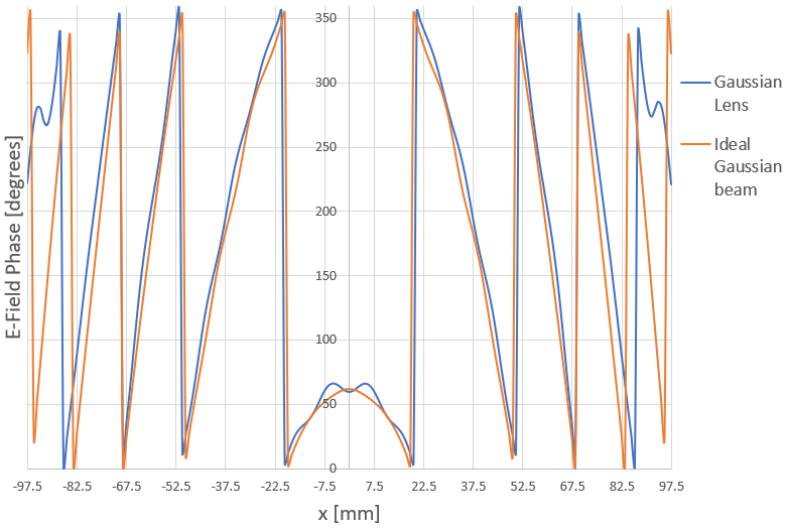

(b) Side view.

Figure 3.4: E-field from GL and horn and from an ideal Gaussian beam produced by a CST-MWS macro.

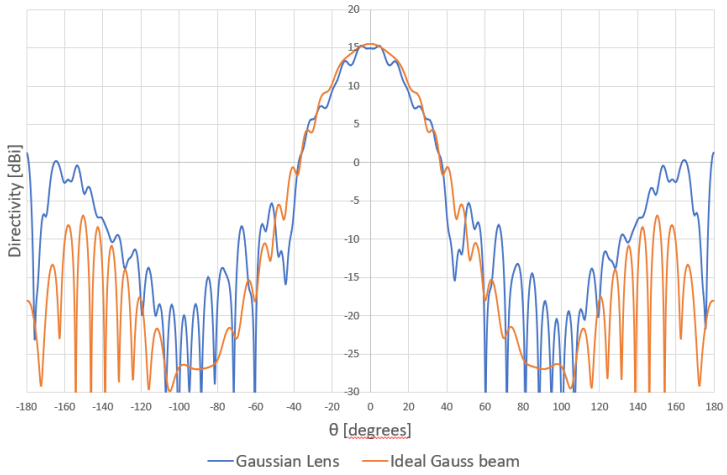

Figure 3.5: Simulated farfield directivity radiation pattern for GL and horn and from an ideal Gaussian beam produced by a CST-MWS macro.

3.2 Unit cell design

The role of the TA Lens is to introduce a phase shift such as to compensate the incident phase and also to introduce a beam tilt. The phase shift is obtained by the use of different unit cells. Two types of cells are used: parallelepipeds with a square base and a varying sized square shaped hole at the center through and through, with equivalent height and base (type 1), as seen in Figure 3.6; and parallelepipeds with a square base with equivalent dimensions and varying height (type 2), as seen in Figure 3.7.

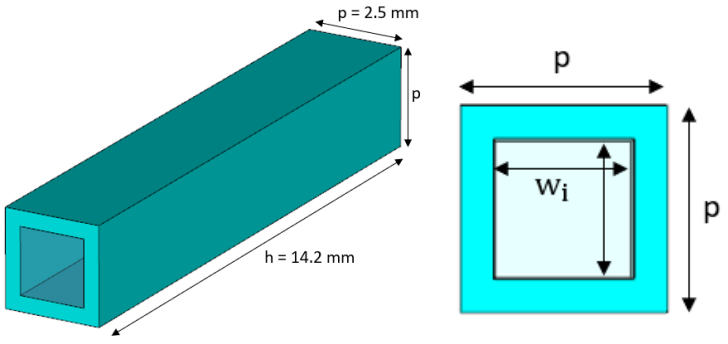

(a) 3D view. **(b)** Front view.

Figure 3.6: Model of type 1 cell.

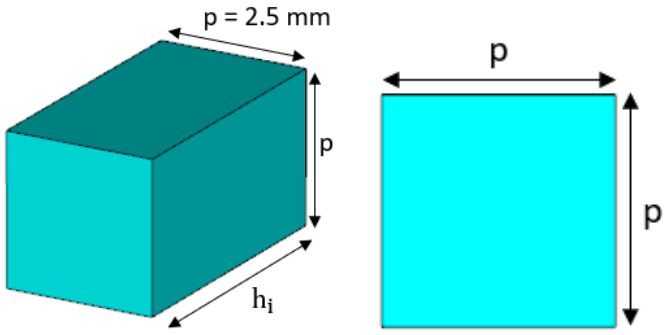

(a) 3D view. **(b)** Front view.

Figure 3.7: Model of type 2 cell.

The unit cells are made of a thermoplastic material with dielectric properties, PLA, with a dielectric constant of $\epsilon_r = 2.9$ and a loss tangent of $\tan\sigma = 0.018$ at 30 GHz.

The type 1 cell should introduce the lowest phase shift when the width of the hole is largest and introduce the largest phase shift when there is no hole, so the phase introduced by the unit cell will vary depending on the size of the hole through it. This largest phase shift of 2π more than a cell of air, is used to determine the height of the type 1 from Equation 3.5.

$$k_0 h\sqrt{\epsilon_r} - k_0 h = 2\pi \Leftrightarrow h = \frac{\lambda}{\sqrt{\epsilon_r} - 1} = 14.2 \tag{3.6}$$

Initially the base length p of unit cell was $\lambda/2$ mm, for a frequency of 30 GHz and thus $\lambda = 10$ mm, as it achieved a range of close to $360°$ of introduced phase while keeping the lens at a constant height. But due to rapid variation of the needed phase to be introduced along part of the x axis of the lens, a smaller unit cell of $p = \lambda/4$ was tested. The type 1 cell for this dimension only achieved a range of $180°$ so a different cell had to be used to achieve the remaining $180°$, the type 2 cell. This cell is also in the shape parallelepiped of the same base length but with no hole, instead the height h of PLA varies, the larger the height the larger the introduced phase shift. Simulations done in CST-MWS, with the two types of cell with length $\lambda/4$ yielded a higher gain than ones with just the type 1 cell with length $\lambda/2$.

To obtain the phase introduced for each valued of w and h the model of each cell was built, separately, in CST-MWS. The boundaries of the cell were set to "Unit Cell", to simulate an infinite array of identical cells. Of course, this method has limitations as it doesn't represent exactly what happens in the actual lens, as the adjacent cells differ from each other, the incidence angle is different depending on the distance to the source, and the lens isn't infinite so doesn't account for edge effects. The simulations used the Frequency Solver Domain and two waveguide ports, one 10 mm away from the top and the other 10 mm from the bottom of the cell. The incidence angle was set to zero, and the perforation width of the the type 1 cell was changed with a parameter sweep of w from 0 to 1.7 mm, and the height of

the type 2 cell was changed with a parameter sweep of h, from 0.4 to 14.1 mm, with a step size of 0.1 mm. The reason for the 0.8 mm difference between the cell length p and the hole length w is due to the nozzle diameter of 0.4 mm of the 3D printer. The value of the unwrapped phase of the resulting S_{21} parameter was obtained for each value of w and h and also for a cell of 14.2 mm height but completely made of vacuum, so the phase introduced by the unit cell was determined by $\phi_{cell} - \phi_{vacuum}$. The cells were picked so as to obtain a stepsize of around $10°$, resulting in 31 different cells in the $[-360°, 0]$ range. If close values of w or h had a close phase output the one which maximized the $|S_{21}|$ parameter was picked.

The phase behaviour of the transmission coefficient of some cells are represented in Figure 3.8 and the amplitude behaviour,$|S_{21}|$, for all the cells is represented in Figure 3.9, with type 1 cells in blue and type 2 cells in orange. Most of type 1 cells have a worse $|S_{21}|$ than type 2 cells, which is expect as they are thicker and have more volume of PLA, but to better visualize this relationship Figure 3.10 shows the $|S_{21}|$ versus the volume of PLA. For cells with larger volumes, cells of type 2, past the maximum height used of ($h = 6.8$ mm) would produce a $|S_{21}|$ larger than type 1 cells, even going beyond -2 dB, making a mixture of the two types of cells a more attractive solution.

Figure 3.11 and Table 3.1 show the phase introduced by each used unit cell. Figure 3.12 shows the phase introduced by the two types of cells versus their varying dimensions, hole width w and cell height h.

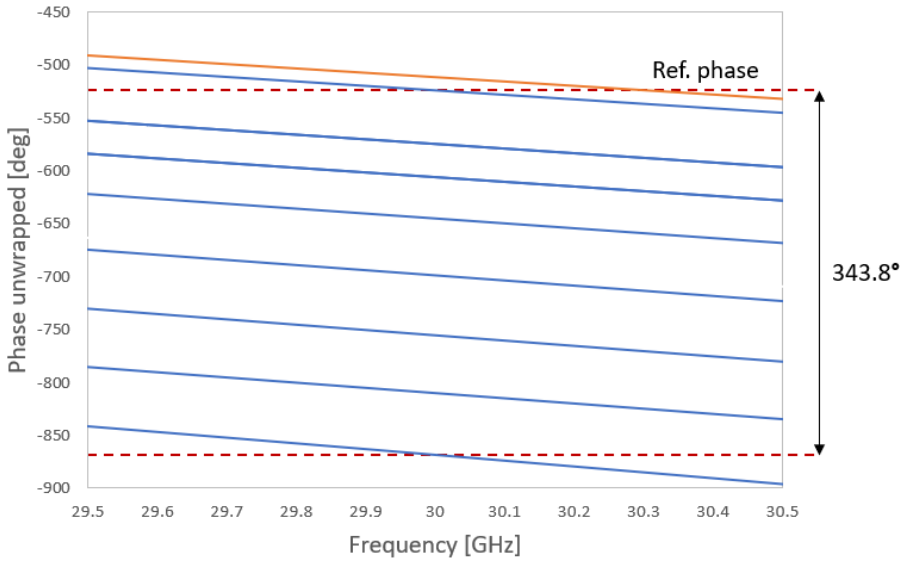

Figure 3.8: Transmission coefficient S_{21} unwrapped phase for a sample of unit cells.

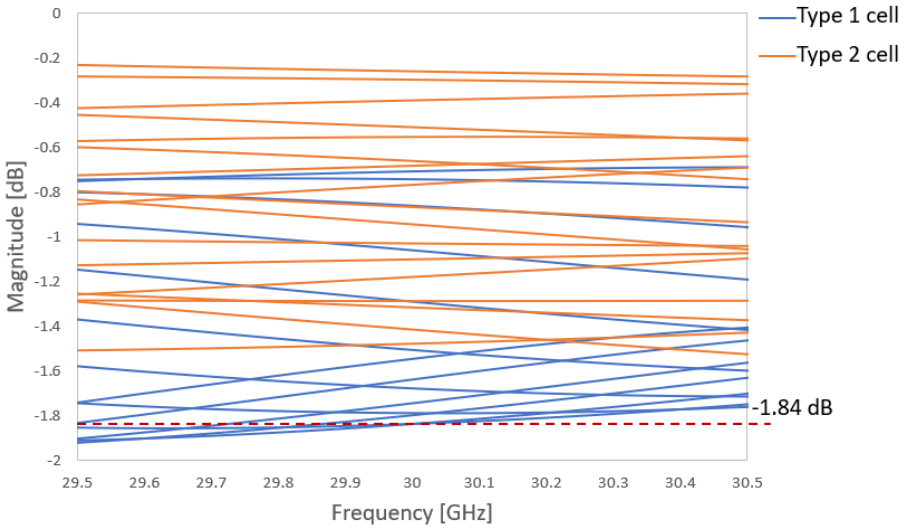

Figure 3.9: Amplitude of the transmission coefficient $|S_{21}|$ for all unit cells.

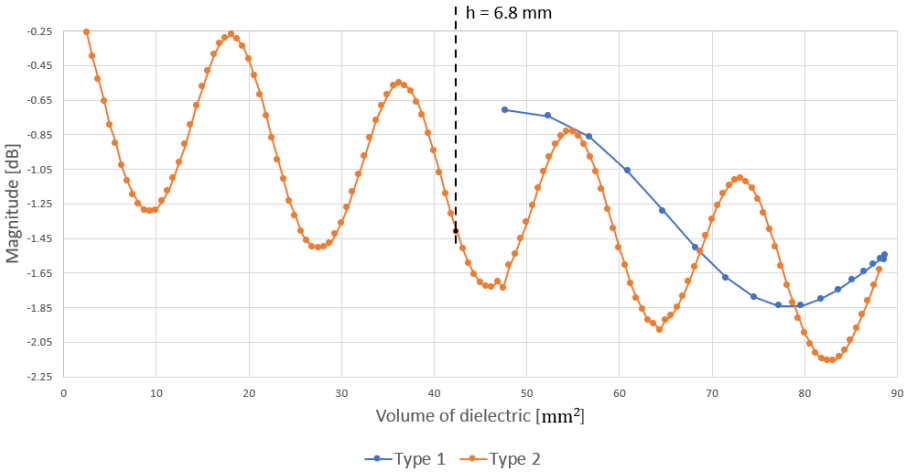

Figure 3.10: Amplitude of the transmission coefficient $|S_{21}|$ versus volume of a cell of type 1 (solid blue curve) and type 2 (solid orange curve).

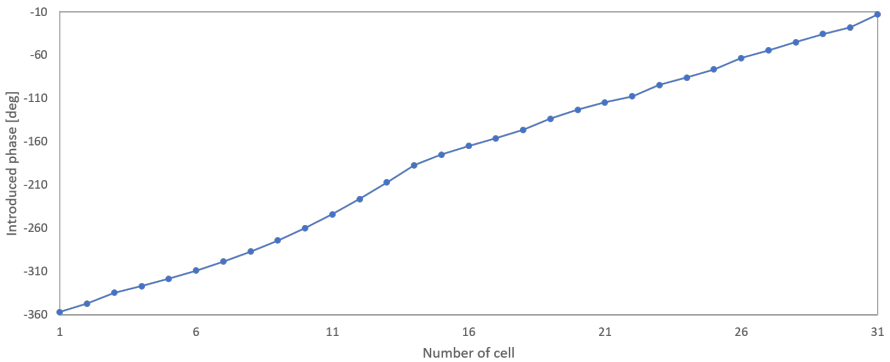

Figure 3.11: Phase introduced by all of the cells.

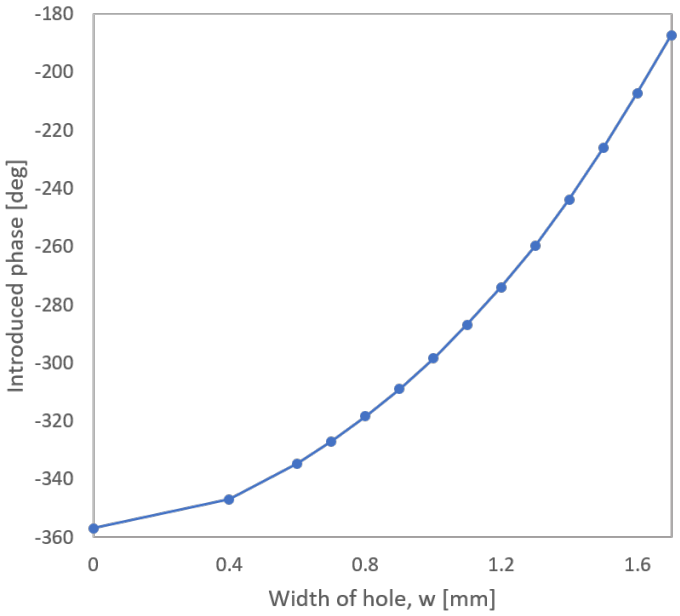

(a) Type 1 cell

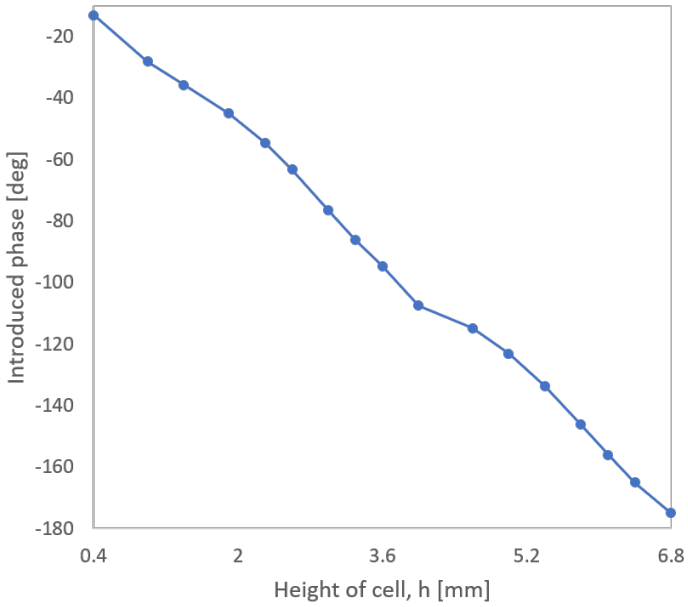

(b) Type 2 cell

Figure 3.12: Phase introduced by the cell versus (a) width of the hole (b) height.

Type of cell	i^{th} cell	$\phi_{cell} - phi_{air}$ [deg]	w [mm]	h [mm]	PLA volume [mm^2]	$\|S_{21}\|$ [dB]
1	1	-356.9	0	14.2	88.8	-1.55
	2	-346.9	0.4	14.2	86.5	-1.64
	3	-334.6	0.6	14.2	83.6	-1.75
	4	-327.0	0.7	14.2	81.8	-1.84
	5	-318.4	0.8	14.2	79.7	-1.84
	6	-309.0	0.9	14.2	77.2	-1.84
	7	-298.5	1.0	14.2	74.6	-1.79
	8	-286.9	1.1	14.2	71.6	-1.68
	9	-274.1	1.2	14.2	68.3	-1.51
	10	-259.8	1.3	14.2	64.8	-1.29
	11	-243.9	1.4	14.2	60.9	-1.06
	12	-226.2	1.5	14.2	56.8	-0.86
	13	-207.2	1.6	14.2	52.4	-0.74
	14	-187.3	1.7	14.2	47.7	-0.71
2	15	-175.0	0	6.8	42.5	-1.42
	16	-165.1	0	6.4	40.0	-0.94
	17	-156.1	0	6.1	38.1	-0.66
	18	-146.3	0	5.8	36.3	-0.55
	19	-133.6	0	5.4	33.8	-0.77
	20	-123.1	0	5.0	31.3	-1.18
	21	-114.8	0	4.6	28.8	-1.48
	22	-107.5	0	4.0	25.0	-1.32
	23	-94.6	0	3.6	22.5	-0.87
	24	-86.1	0	3.3	20.6	-0.51
	25	-76.5	0	3.0	18.8	-0.30
	26	-63.3	0	2.6	16.3	-0.39
	27	-54.5	0	2.3	14.4	-0.68
	28	-45.0	0	1.9	11.9	-1.10
	29	-35.7	0	1.4	8.8	-1.29
	30	-28.2	0	1.0	6.3	-1.03
	31	-13.1	0	0.4	2.5	-0.26

Table 3.1: Dimensions and relative phase and amplitude of the transmission coefficient of each cell.

3.3 Full wave simulations of the transmit-array

In order to simulate the TA in full wave the models of the TA lens was designed by first assigning a phase shift to each cell, as explained in Section 3.2, second by assigning a phase shift for each point of the lens, from the Equation 1.1 and finally generating the lens using a VBA macro for CST-MWS. Two different TA lenses were constructed, one for a spherical wave incidence, shown in Figure 3.13, the other for a Gaussian beam incidence, shown in Figure 3.14, to compare the performance of the two antennas.

The dimensions used for the design of the lens were the same for both lenses as in [3], that is, 195$\times$145 mm.

The focal distance used to design both lenses was of $F = 110$ mm but instead of this being the distance from the source to the base of the lens, it is the distance to the middle of the lens thickness and thus the distance to the base is 102.9 mm. This was done because the main lobe at the central position was not symmetric as was expected, so a few adjustments in the lens position were experimented with to resolve this problem, which in the end yielded a higher directivity and a ”straight” main lobe in the central position. This might have been due to the lens being quite thicker than what is usually used. Additionally, the TA lens is inverted (the base is facing away from the feed) also due to better results obtained from simulations.

The results are divided into four subsections, according to the TA model used. These are, in order, spherical wave, ideal Gaussian beam, Gaussian beam and Gaussian beam with support structure, which was the model used as base for the prototype fabrication.

Due to the models in CST-MWS being somewhat large and the limited resources of the workstation running the simulations and the amount of hours they took to finish, the number of mesh cells had to be reduced, in the mesh properties menu and in the boundary menu, as since the TA lenses are symmetrical in the Y length (shortest one) the simulations were done considering a symmetry around the plane $Y = 0$, reducing the number of mesh cells by half. The final simulations presented here had around 66 to 261 million mesh cells, depending on the model.

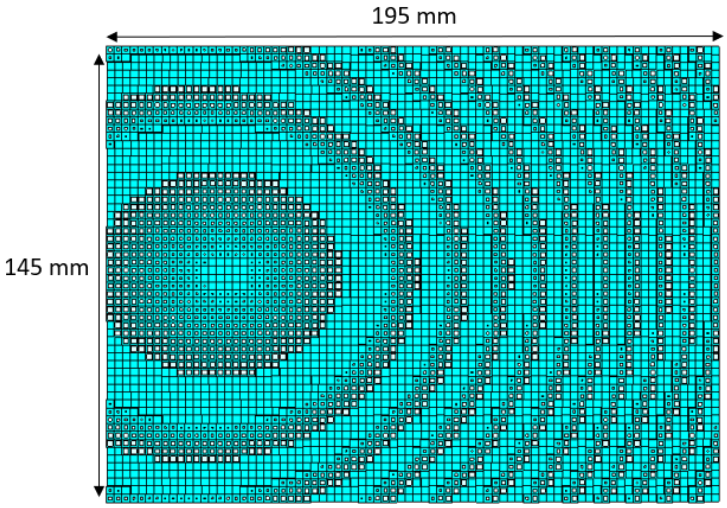

Figure 3.13: Front view of the spherical wave TA lens model.

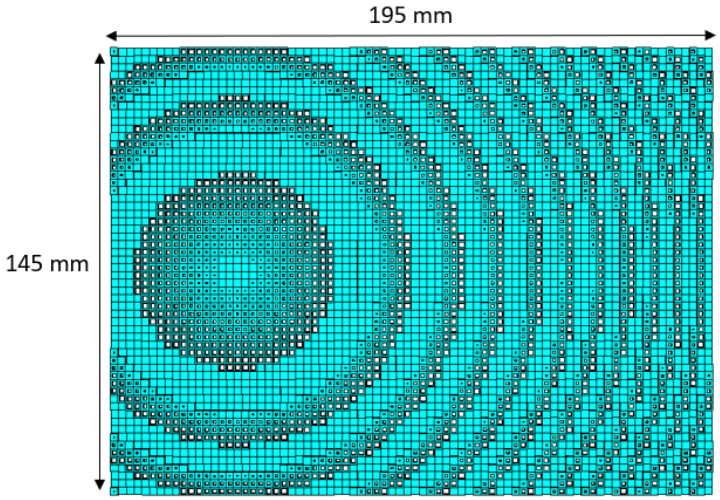

Figure 3.14: Front view of the Gaussian beam TA lens model.

3.3.1 Spherical wave transmitarray

This TA is designed for a spherical wave feed and thus only the horn is used as the feed. The model is shown in Figure 3.15, the distance from the horn to the base of the lens is 102.9 mm, as explained above.

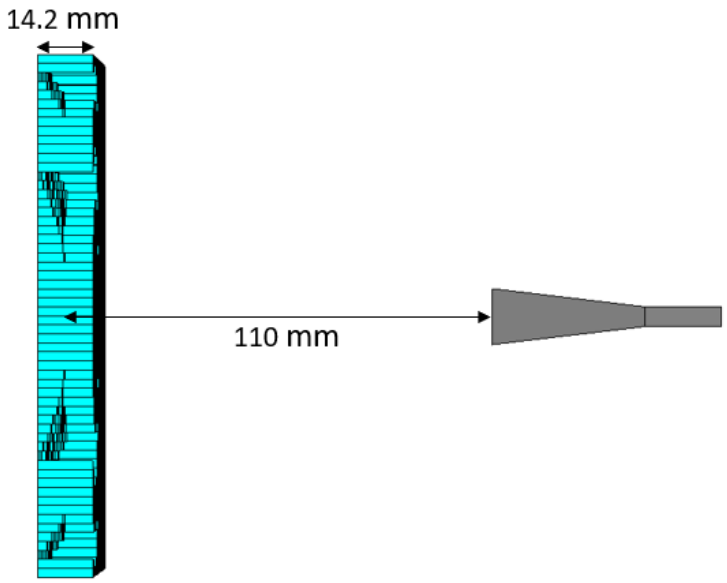

Figure 3.15: Side view of the simulation model of the spherical wave TA

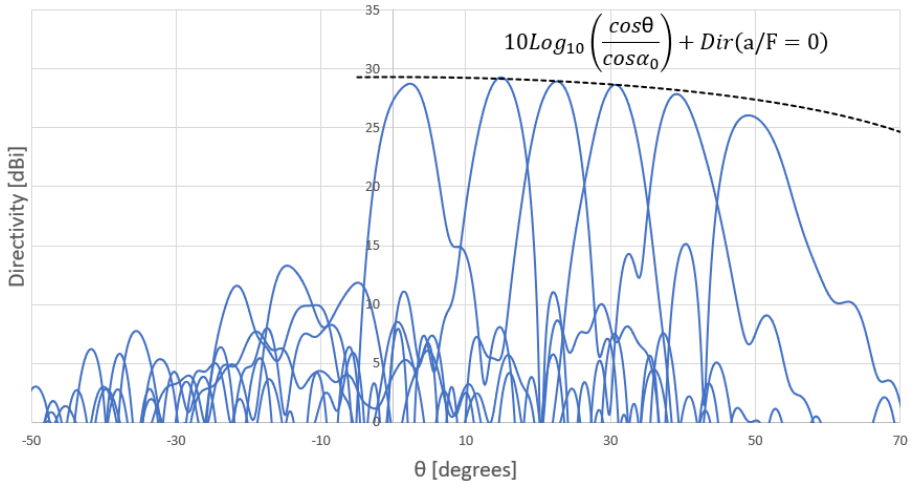

Figure 3.16: Simulated farfield directivity radiation pattern for the spherical wave feed offset in the interval $a/F \in [-0.27, 0.55]$ with 0.09 step size. The dashed black curve represents the maximum normalized directivity as function of θ considering $\phi_{nl} = 0$.

Figure 3.16 shows the directivity radiation pattern for the spherical wave TA. The dashed black curve represents the maximum normalized gain if nonlinear phase error was zero. The effect of beam aberrations in the positive feed displacements (tilt angles below 30 degrees) is not as obvious as in the results of the PO simulations shown in Figure 2.4, as there doesn't seem to be any directivity decay, although some positions, in the whole interval, show high SLL on the main beam.

There is a lot of high side-lobe radiation being transmitted between -30 and 0 degrees, which will be addressed further.

The results for each feed displacement position are summarized in Table 3.2.

3.3.2 Ideal Gaussian beam

Before testing the TA lens with the Gaussian feed described in Section 3.1, the solver for a Gaussian beam in the CST-MWS macro was used as the feed. The parameters were the same used to make the Gaussian lens, frequency of 30 GHz, beam waist $w_0 = 6.5$ mm and focal distance $F_1 = -80$ mm. This means that at the exit of the solver, the beam is calculated as if it is at a distance of 80 mm from the beam waist. As the focal distance for the TA lens is $F = 110$ mm it should be at a distance of 30 mm from the feed. Instead of it being the distance to the base of the TA lens it is to the middle of the lens, as explained previously. So the distance between the TA lens and the feed is 22.9 mm instead of 30 mm, as shown in Figure 3.17.

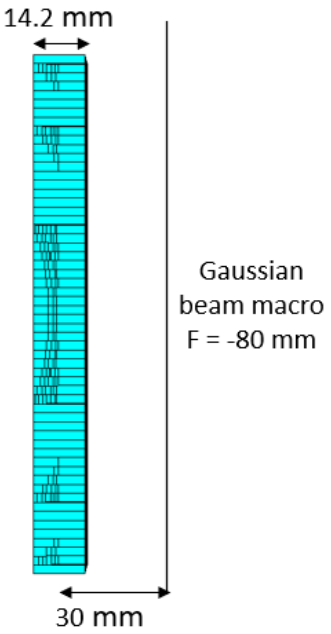

Figure 3.17: Side view of the TA model with the ideal Gaussian beam solver as feed.

Figure 3.18 shows the simulated directivity radiation pattern and Table 3.2 shows a summary of the results. Again, the dashed black curve represents the maximum normalized gain if non linear nonlinear phase error was zero. This TA produces a well defined main lobes and low SLL for feed offset different than zero.

There is a lot of high sidelobe radiation being transmitted in the $-30°$ and $0°$ zone, which is partly due to the large thickness of the TA lens. Simulations were done with a TA lens of another material of a higher permittivity $\epsilon_r = 12$, instead of the $\epsilon_r = 2.9$ of PLA. This lens had a reduced maximum thickness,

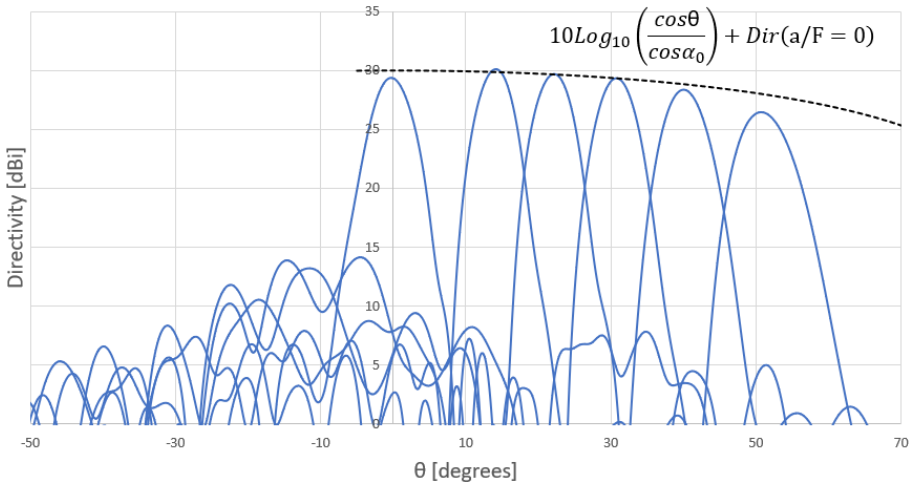

Figure 3.18: Simulated farfield directivity radiation pattern for the ideal Gaussian beam feed offset in the interval $a/F \in [-0.27, 0.55]$ with 0.09 step size. The dashed black curve represents the maximum normalized directivity as function of θ considering $\phi_{nl} = 0$.

of 4 mm instead of 14.2 mm and produced quite lower sidelobes, in that region, as seen in Figure 3.19.

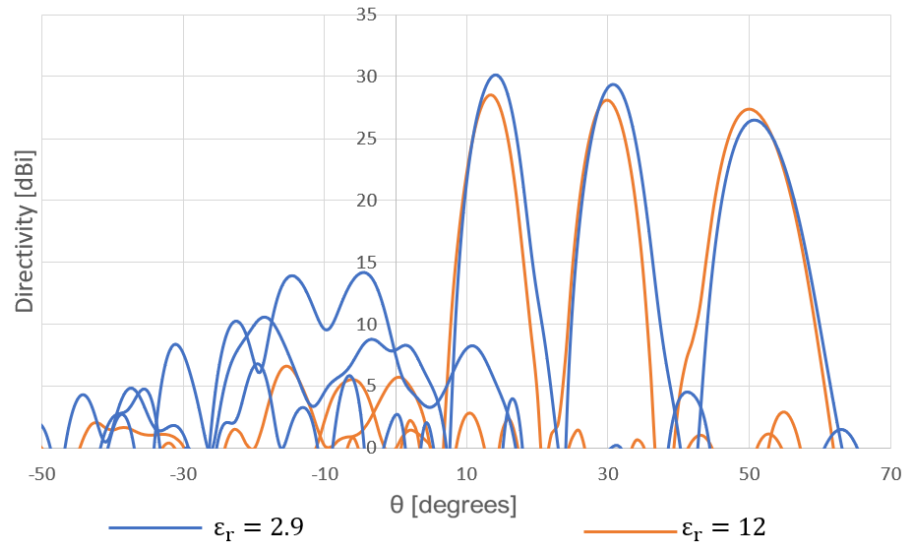

Figure 3.19: Simulated farfield directivity radiation pattern for the ideal Gaussian beam feed offset for $a/F = [-0.27, 0, 0.27]$ for a lens made of two dielectric materials.

3.3.3 Gaussian beam transmitarray

The macro was then replaced with the designed Gaussian beam feed so the TA could be simulated. The model of the TA lens and the feed of the Gaussian lens and the horn were placed as shown in Figure 3.20 to run a full-wave simulation in CST-MWS. The mouth of the horn is at a distance of 80 mm of the base of the Gaussian lens and at a distance of 110 mm of the center of the TA lens. As explained above,

the focal distance of 110 mm is to the center of the lens, so the horn is 102.9 mm away from the TA lens instead of 110 mm and the lens is inverted.

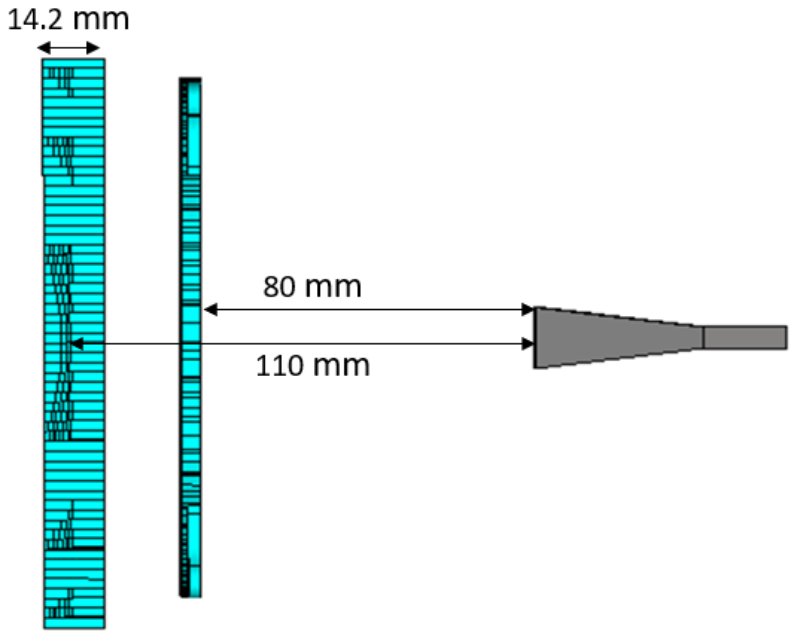

Figure 3.20: Side view of the simulation model of the Gaussian beam TA

Figure 3.21 shows the simulated directivity radiation pattern and Table 3.2 shows a summary of the results. The TA with the designed Gaussian beam feed shows a slight decrease in the directivty of the main lobes from the TA with the ideal Gaussian beam feed. Otherwise, there are no significant differences.

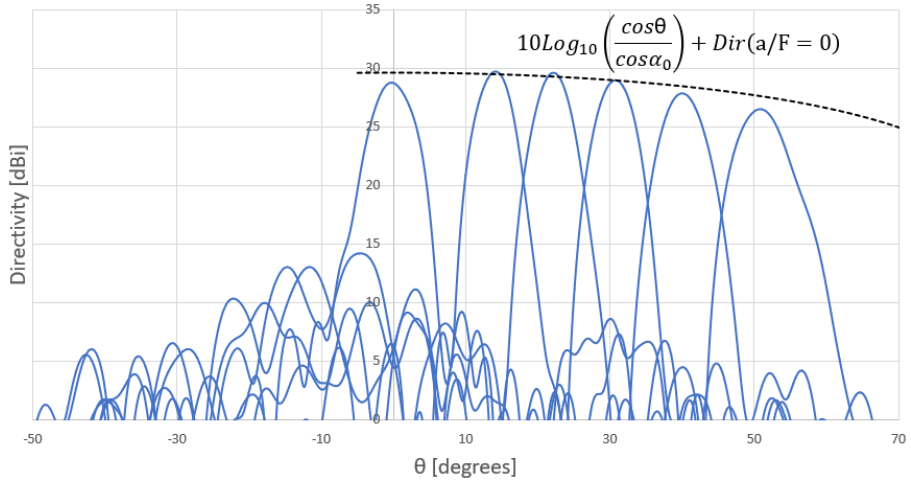

Figure 3.21: Simulated farfield directivity radiation pattern for the Gaussian beam feed offset in the interval $a/F \in [-0.27, 0.55]$ with 0.09 step size. The dashed black curve represents the maximum normalized directivity as function of θ considering $\phi_{nl} = 0$.

The simulations above were also used to obtain the radiation pattern for frequencies 1 GHz around the central frequency 30 GHz, in steps of 0.25 GHz. The gain against frequency responses for different feed offsets a is represented in Figure 3.22 and the main lobe zenith angle versus the frequency in Figure 3.23. Both frequency responses are fairly constant, with a difference lower than $|1|$ dB from the central position's gain and a difference lower than $|1.5|$ degrees from the central position's angle.

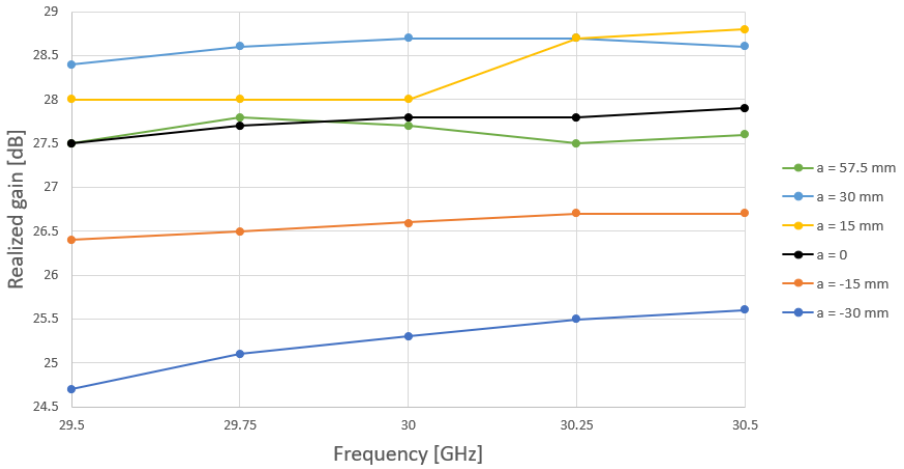

Figure 3.22: Frequency responses of the main beam realized gain for different feed offsets.

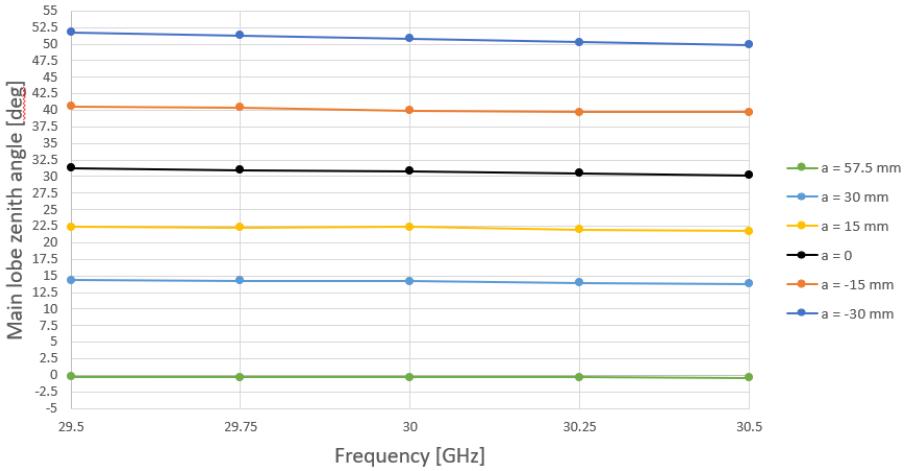

Figure 3.23: Frequency response of the main beam tilt for different feed offsets.

3.3.4 Gaussian beam transmit-array with support structure

A structure was designed to support and position the lenses that will be fabricated to obtain the experimental results. The structure is of the same material as the two lenses, PLA, so it can also be 3D

Table 3.2: Results of TA simulation with different feeds.

Feed offset		Ideal Gaussian	Gaussian	Spherical
a = -30 mm	**Directivity [dBi]**	26.5	26.5	26.1
	θ **max [deg]**	50.8	50.8	49.0
	SLL [dB]	-18.4	-24.8	-11.0
a = -15 mm	**Directivity [dBi]**	28.4	27.9	27.9
	θ **max [deg]**	40.0	40.0	39.1
	SLL [dB]	-27.5	-25.8	-13.6
a = 0 mm	**Directivity [dBi]**	29.4	29.0	28.7
	θ **max [deg]**	30.8	30.8	30.7
	SLL [dB]	-25.5	-26.6	-23.6
a = 15 mm	**Directivity [dBi]**	29.7	29.6	28.9
	θ **max [deg]**	22.2	22.4	22.6
	SLL [dB]	-23.7	-23.4	-21.9
a = 30 mm	**Directivity [dBi]**	30.1	29.7	29.3
	θ **max [deg]**	14.2	14.2	14.8
	SLL [dB]	-28.1	-22.4	-18.2
a = 57.5 mm	**Directivity [dBi]**	29.4	28.8	28.8
	θ **max [deg]**	-0.3	-0.3	2.3
	SLL [dB]	-22.1	-19.6	-20.5

printed. The full TA with the structure, represented in Figures 3.24 to 3.27, was designed and simulated in CST-MWS. With the support structure, the total antenna dimensions are 195$\times$175.4 mm with a height of 178.6 mm.

The radiation pattern of this model is superimposed to the one with no support structure, in Figure 3.28 to understand the impact of the support structure.

The radiation pattern of the TA with the support structure (solid brown curves) seen in Figure 3.28, shows no significant differences to the model with no support structure (solid blue curves). The results are summarized in the Table 3.3.

In the next chapter the result of the simulations with the support structure will be compared to the experimental results.

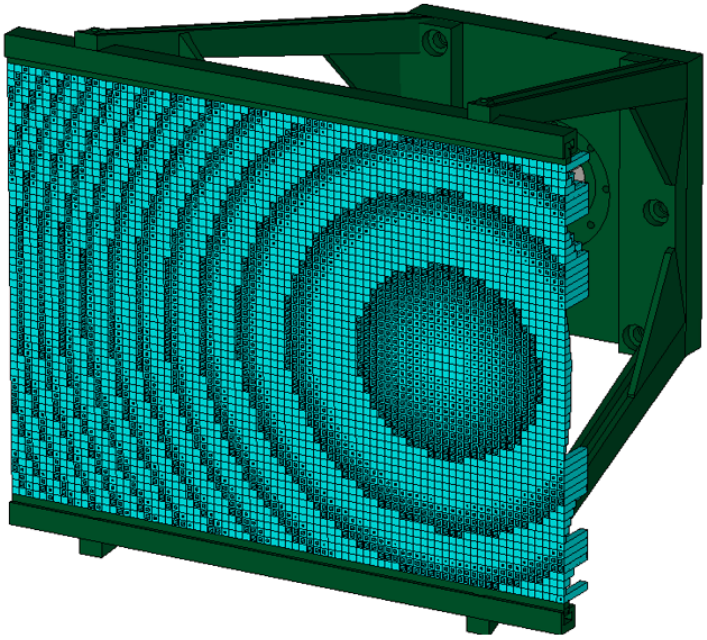

Figure 3.24: Model of the TA with the support structure (green).

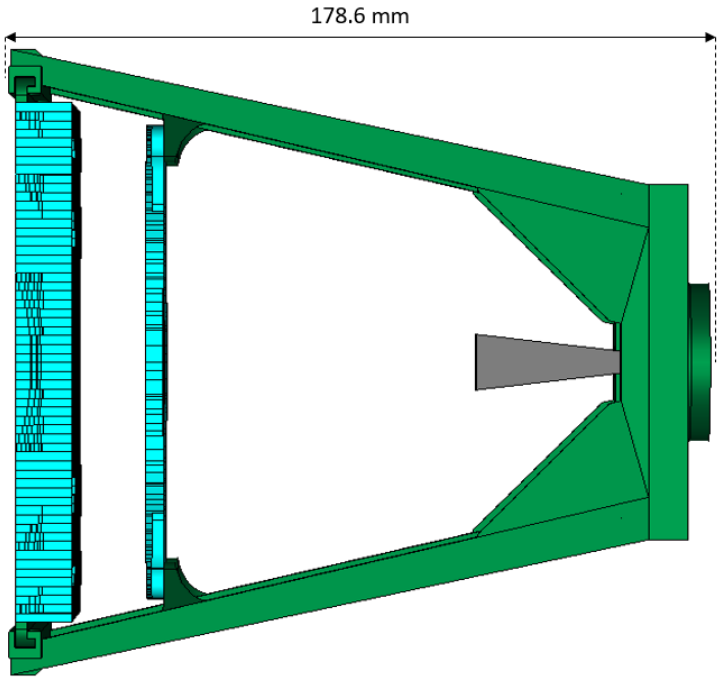

Figure 3.25: Model of the TA with the support structure (green).

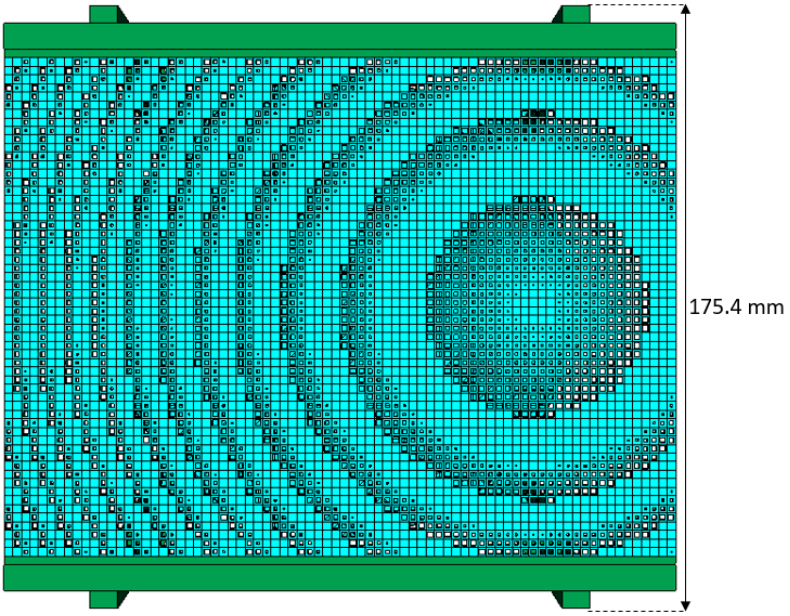

Figure 3.26: Model of the TA with the support structure (green).

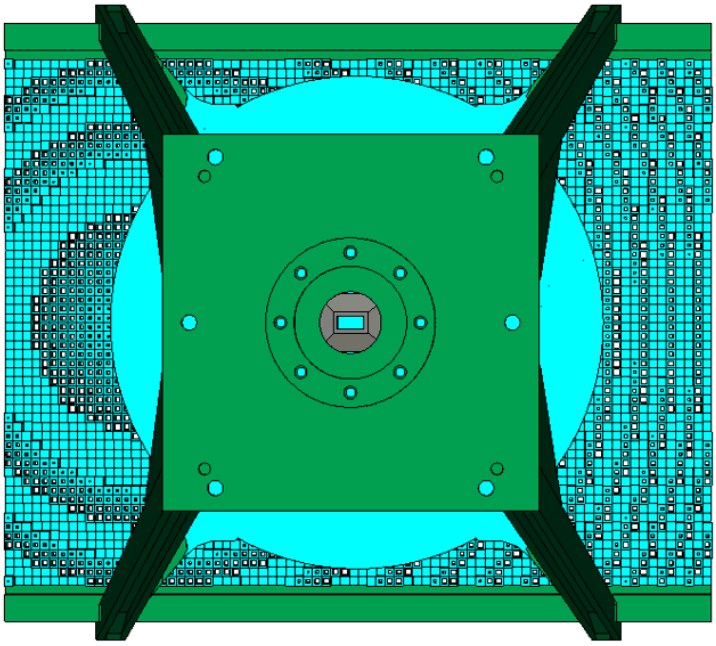

Figure 3.27: Model of the TA with the support structure (green).

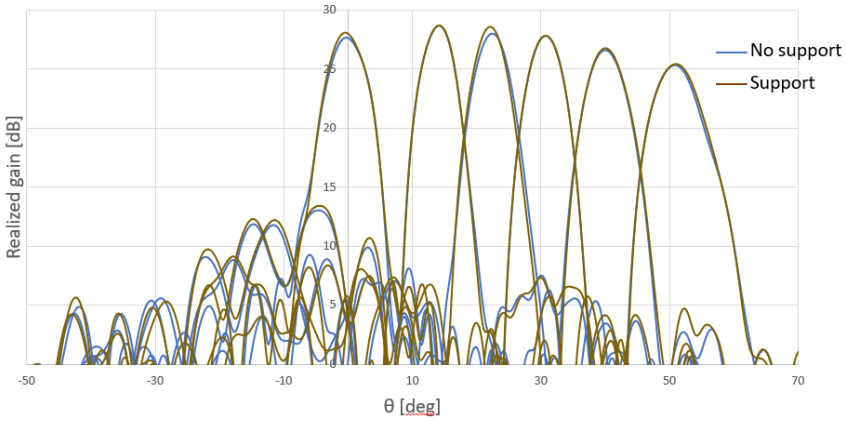

Figure 3.28: Realized gain for the TA without support structure (blue) and with support structure (brown).

Table 3.3: Results of Gaussian beam TA simulation with and without support structure.

Feed offset		Support	No support
a = -30 mm	**Real. Gain [dB]**	25.4	25.3
	θ **max [deg]**	51.0	50.8
	SLL [dB]	-23.4	-24.8
a = -15 mm	**Real. Gain [dB]**	26.8	26.6
	θ **max [deg]**	41.0	40.0
	SLL [dB]	-24.8	-25.8
a = 0 mm	**Real. Gain [dB]**	27.8	27.8
	θ **max [deg]**	30.8	30.8
	SLL [dB]	-24.8	-26.6
a = 15 mm	**Real. Gain [dB]**	28.6	28.0
	θ **max [deg]**	22.1	22.4
	SLL [dB]	-21.8	-23.4
a = 30 mm	**Real. Gain [dB]**	28.7	28.7
	θ **max [deg]**	14.2	14.2
	SLL [dB]	-21.7	-22.4
a = 57.5 mm	**Real. Gain [dB]**	28.1	27.7
	θ **max [deg]**	-0.4	-0.3
	SLL [dB]	-21.5	-19.6

4

Experimental Results

Contents

4.1 Prototype fabrication and assembly

The prototypes of the GL and the support structure were fabricated by using the 3D CAD models used in the simulations in Chapter 3. The prototypes were then printed layer by layer in an additive layer process by heating the thermoplastic material PLA to its melting point and then extruding it through the nozzle of the 3D printer onto its base platform. As each layer of the prototype is completed, the base is lowered to provide space for the next layer of thermoplastic until the printing is complete. The minimum height for the layer was of 0.3 mm, as lower values could compromise the integrity of GL. Due to an error in the assembling of the prototype, the focal distance for both lenses in the prototype is 7 mm lower than that of the simulated model. This discrepancy was noted too late, after all the anechoic chamber measurements had been performed. However, the difference in focal distance was applied to the CST-MWS model and a simulation was performed for the 30 mm feed displacement and the radiation patterns, shown in Figure 4.1, compared with the previous ones, showing very little difference between them and negligible difference both between the maximum gains (below 0.5 dBi) and its tilt (below $0.5°$) for the same frequencies.

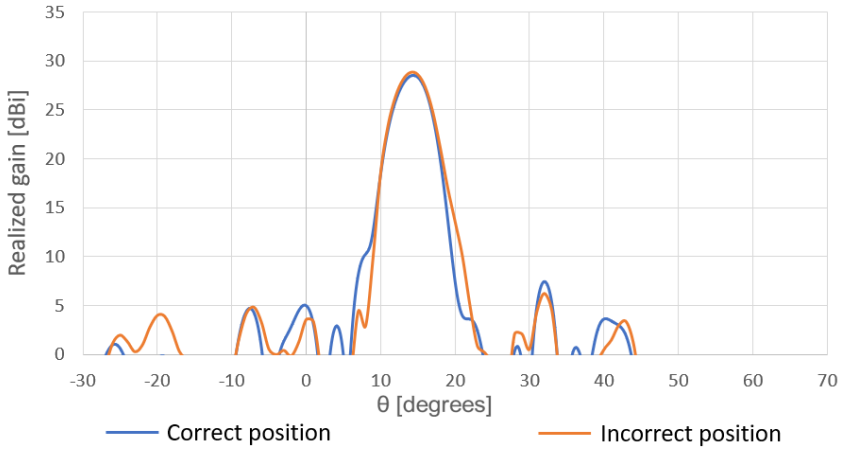

(a) 29.5 GHz

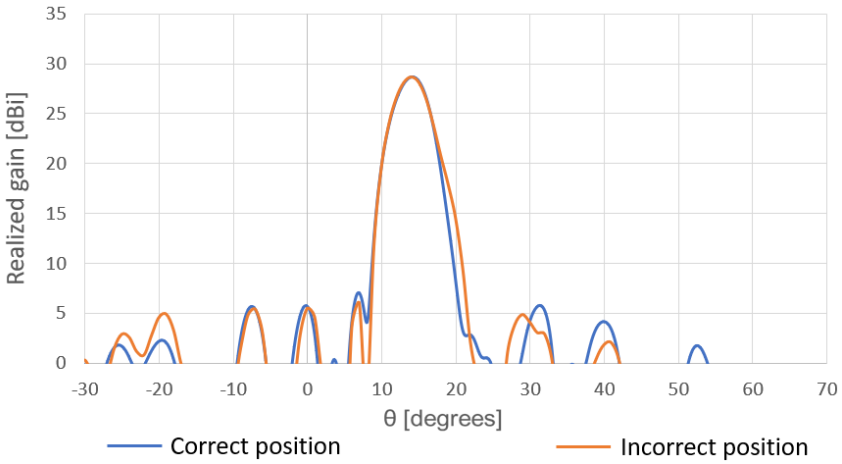

(b) 30.0 GHz

Figure 4.1: Simulated farfield realized gain of TA for the correct lenses' positions (blue) and the positions used in the prototype measurements (orange).

4.2 Gaussian beam feed

First, measurements of the farfield radiation pattern were taken, for the pyramidal horn 22240-15 alone and for frequencies 29.5 to 30.5 GHz in 0.5 GHz increments, in two polarizations, E-field (horizontal polarization) and H-field (vertical polarization). Then the support structure (without the two sliding parts) as seen in Figure 4.2, was placed and the measurements for the H-field were repeated, so as to quantify its influence. The farfield radiation pattern for the horn with and without support structure are represented in Figure 4.3 and it shows negligible difference between the two setups.

A constant value was added to the measured realised gain pattern so as to achieve a maximum realised gain of 14.1 dB of the standard horn 22240 for 30 GHz.

The 3D printed GL made of PLA was then mounted onto the support structure like the model used in simulations, shown in Figures 3.24- 3.27 but without the TA lens, and again, the farfield radiation pattern was measured for the two horn polarizations, E and H field. Figure 4.4 shows the feed prototype in the anechoic chamber and Figure 4.6 shows the simulated and measured H plane farfield realized gain radiation pattern of the feed.

The measured realized was calculated as

$$(G_{antenna})_{dB} = (G_{horn})_{dB} - (|S21_{horn}|)_{dB} + (|S21_{lens}|)_{dB} \tag{4.1}$$

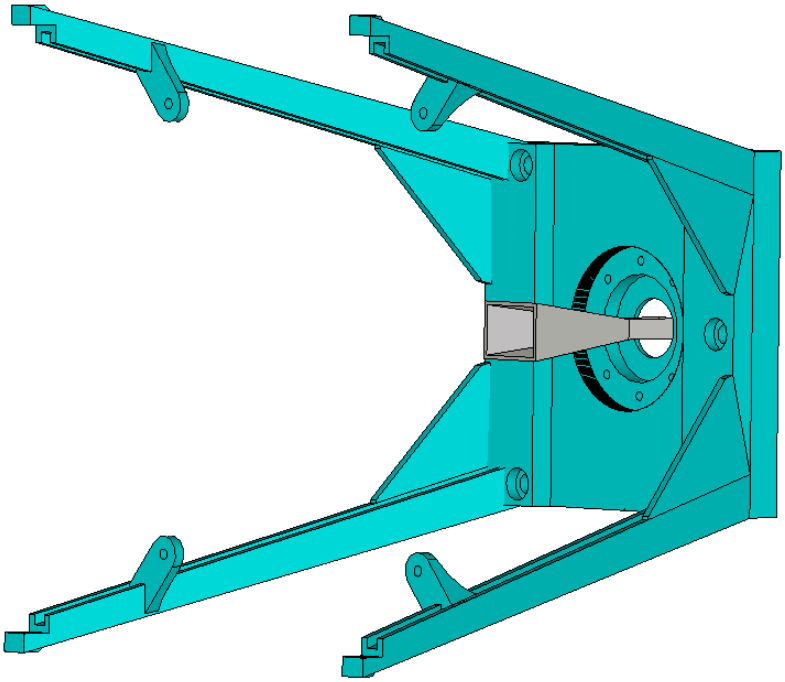

(a) CST-MWS model.

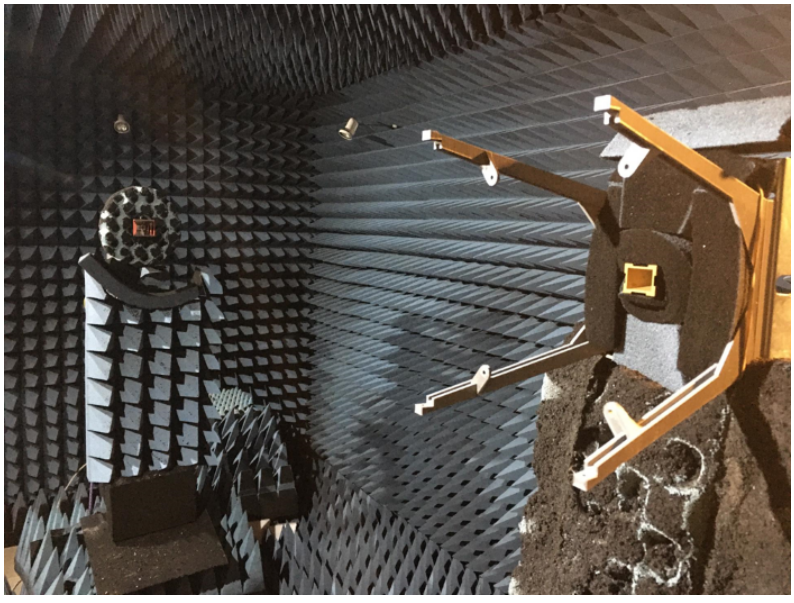

(b) Prototype.

Figure 4.2: Horn with the support structure's poles.

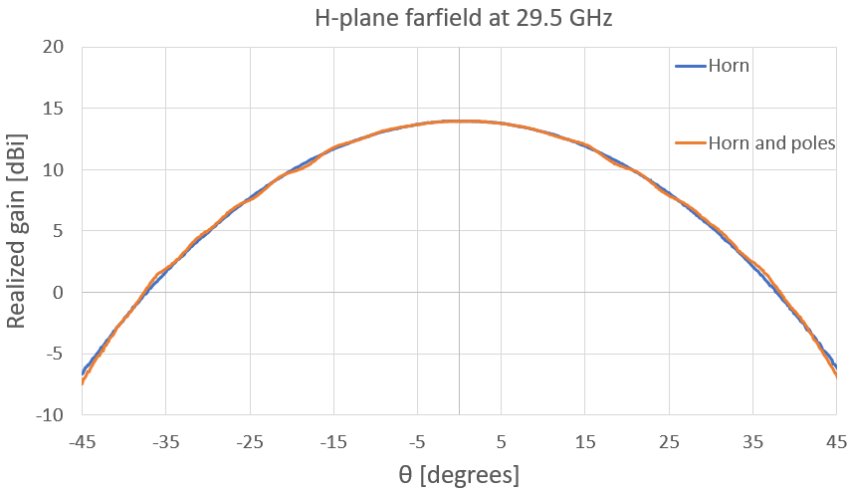

(a) 29.5 GHz

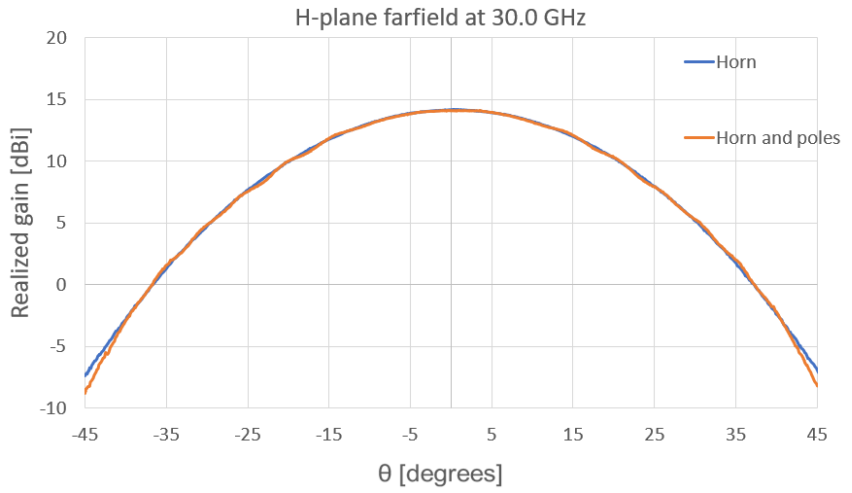

(b) 30.0 GHz

Figure 4.3: H-plane farfield realized gain of horn with and without the support structure poles.

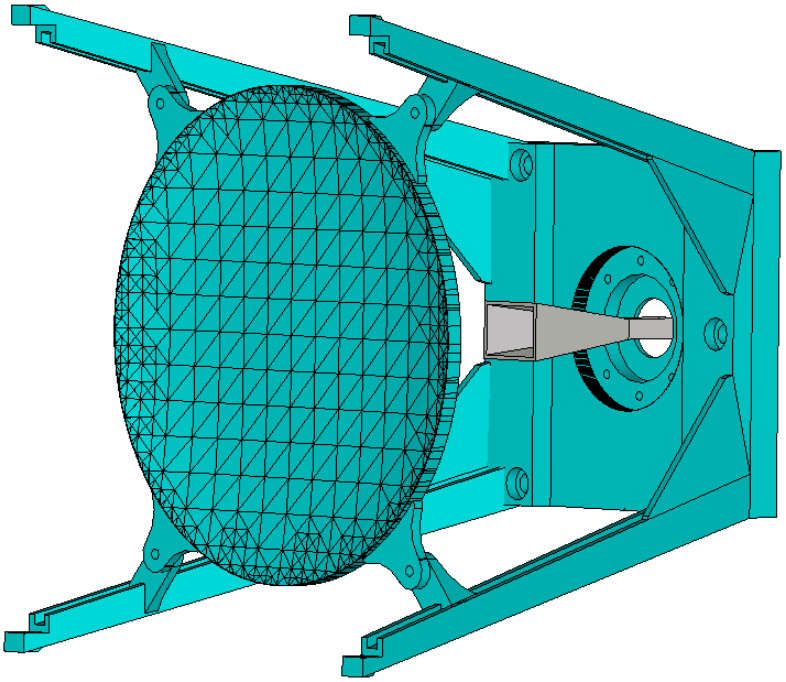

(a) CST-MWS model.

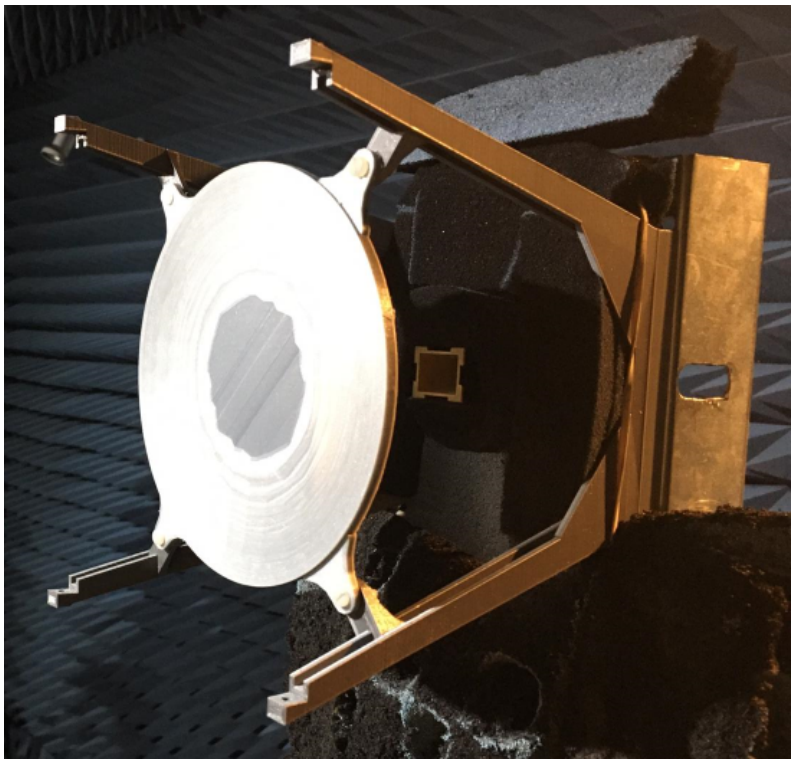

(b) Prototype.

Figure 4.4: Setup of the Gaussian beam feed with the support structure's poles.

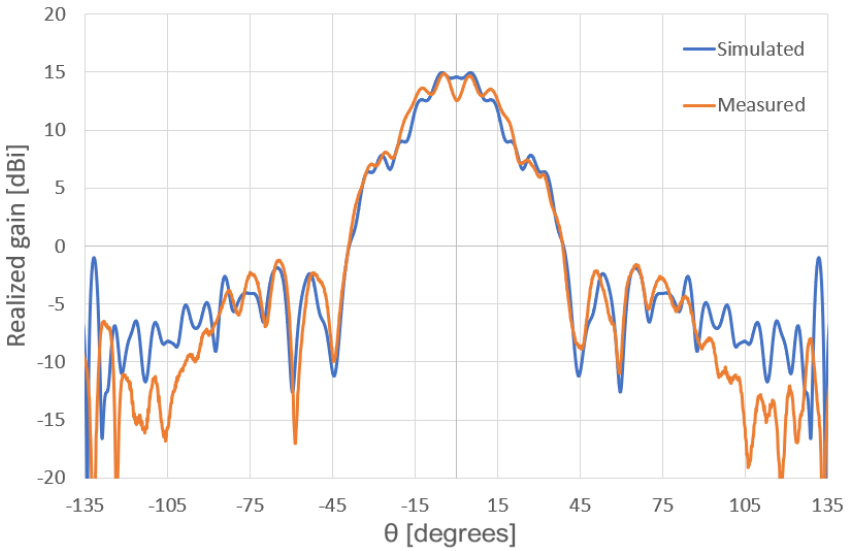

(a) 29.5 GHz

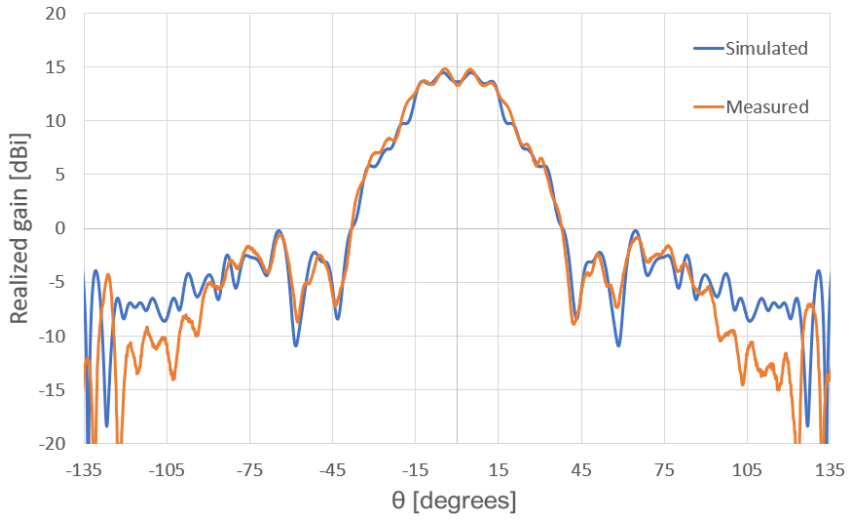

(b) 30.0 GHz

Figure 4.5: E-plane farfield realized gain of feed prototype and simulations.

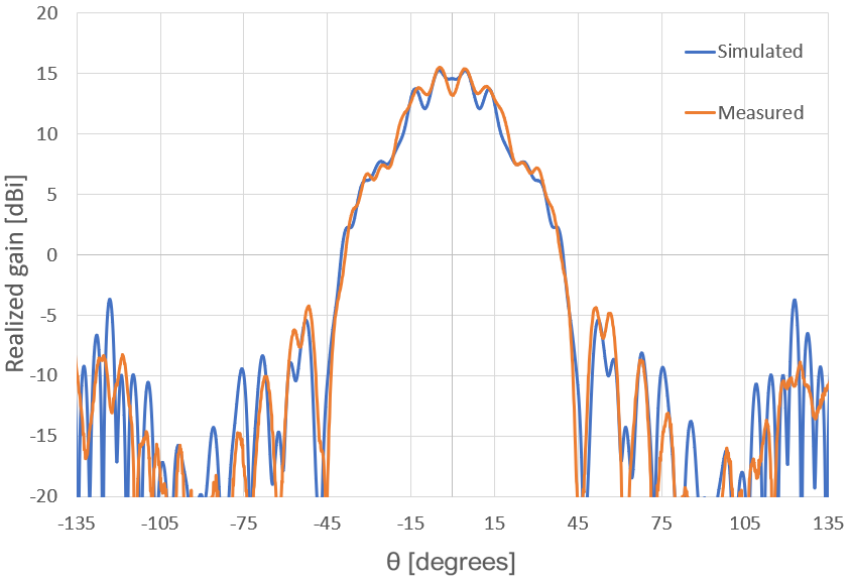

(a) 29.5 GHz

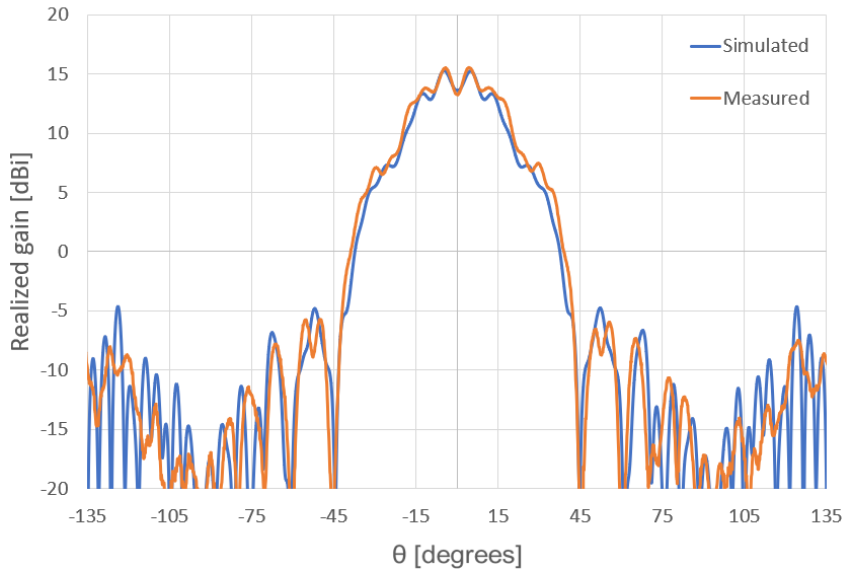

(b) 30.0 GHz

Figure 4.6: H-plane farfield realized gain of feed prototype and simulations.

4.3 Transmit-array measurement results

The prototype of the TA lens was fabricated using the same method described previously. Using the 3D CAD models used in the simulations in Chapter 3 the TA lens prototype was 3D printed in PLA, with the dimensions, 195×145 mm and maximum and minimum thickness of 14.2 mm and 0.4 mm respectively. It was possible to obtain perforations from 0.1 to 0.7 mm although some imperfections might be present in the prototype as the nozzle used only permitted a precision of 0.4 mm and the extruded material did not always set evenly.

The 3D printed TA was mounted onto the support structure and the farfield radiation pattern was measured for the two horn polarizations, E and H-field. Figure 4.7 shows the feed prototype in the anechoic chamber and Figure 4.8 shows the simulated and measured H-plane farfield realized gain radiation pattern of the feed for 30 GHz and feed displacements from -30 mm to 57.5 mm. The feed displacement was achieved by sliding the TA lens along the support structure.

Table 4.1: Results of TA simulation with different feeds.

		29.5 GHz			30.0 GHz		
Feed offset		Sim.	Meas.	Dif.	Sim.	Meas.	Dif.
a = -30 mm	**R. gain [dBi]**	25.0	23.3	1.7	25.4	23.9	1.5
	θ **max [deg]**	52.1	53.1	1.0	51.0	51.8	0.8
	SLL [dB]	-22.0	-22.1	0.1	-31.2	-21.5	-9.7
a = -15 mm	**R. gain [dBi]**	26.6	25.0	1.6	26.8	25.3	1.5
	θ **max [deg]**	40.7	41.5	0.8	40.1	40.9	0.8
	SLL [dB]	-26.1	-20.5	5.6	-24.8	-20.4	4.4
a = 0 mm	**R. gain [dBi]**	27.2	26.5	0.7	27.8	26.7	1.1
	θ **max [deg]**	31.3	32.2	0.9	30.8	31.8	1.0
	SLL [dB]	-25.0	-23.9	1.1	-24.8	-24.0	0.8
a = 15 mm	**R. gain [dBi]**	28.0	27.0	1.0	28.6	27.2	1.4
	θ **max [deg]**	22.5	23.8	1.3	22.1	23.5	1.4
	SLL [dB]	-23.7	-20.7	3.0	-21.8	-19.4	2.4
a = 30 mm	**R. gain [dBi]**	28.5	27.8	0.7	28.7	27.7	1.0
	θ **max [deg]**	14.4	15.5	1.1	14.2	15.0	0.8
	SLL [dB]	-21.0	-19.2	1.8	-21.7	-16.8	4.9
a = 57.5 mm	**R. gain [dBi]**	27.7	26.8	0.9	28.1	26.7	1.4
	θ **max [deg]**	-0.2	0.1	0.3	-0.4	0.2	0.6
	SLL [dB]	-18.8	-19.3	0.5	-21.5	-19.0	2.5

Comparing the simulated and measured results of the radiation pattern in Figure 4.8 it can be seen that the TA behaves as expected. There are small chances encountered in the measured results. There is a slight difference in the tilt however it is consistent for all the positions so it is most likely due to a misalignment in the prototype model. Some aberrations can be seen but not very high. The gain is also lower but that is to be expected due inaccuracies in the manufacturing and assembling of the prototype and unaccounted losses in the simulations.

The simulations show a scan loss of 3.5 dB for 29.5 GHz and 3.3 dB for 30 GHz. The measurements show a worse scan loss of 4.5 dB for 29.5 GHz and 3.8 dB for 30 GHz. The maximum values of the measured cross component, shown in Figure 4.9, are at least 20 dB inferior to the co component.

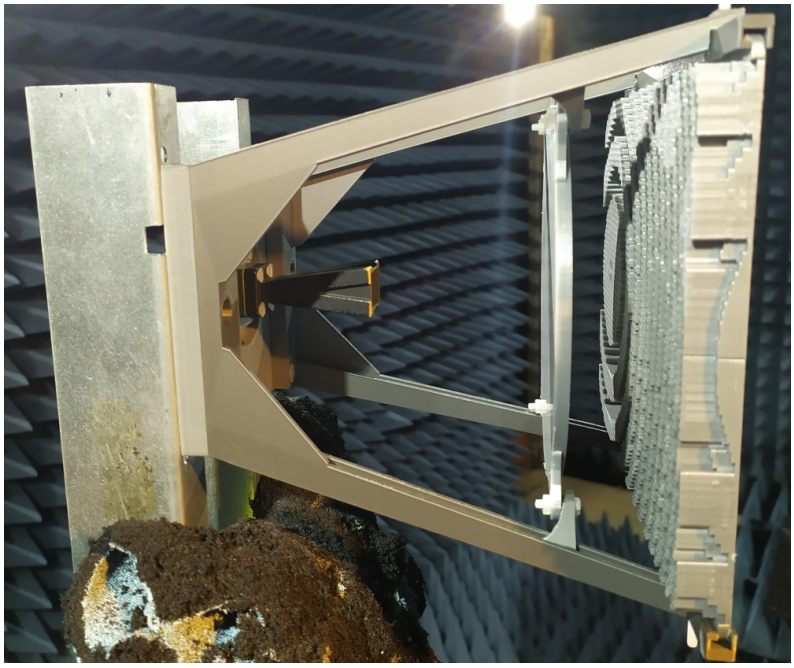

(a) Side view.

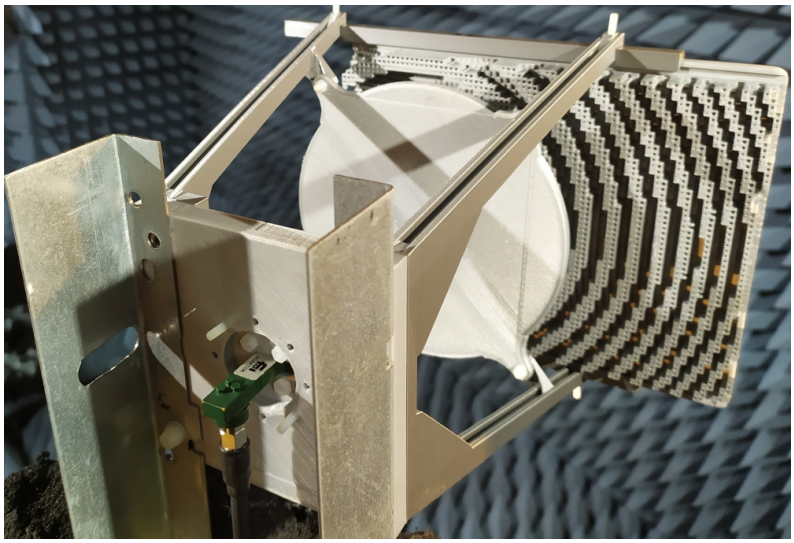

(b) Back view.

Figure 4.7: TA prototype mounted in the anechoic chamber.

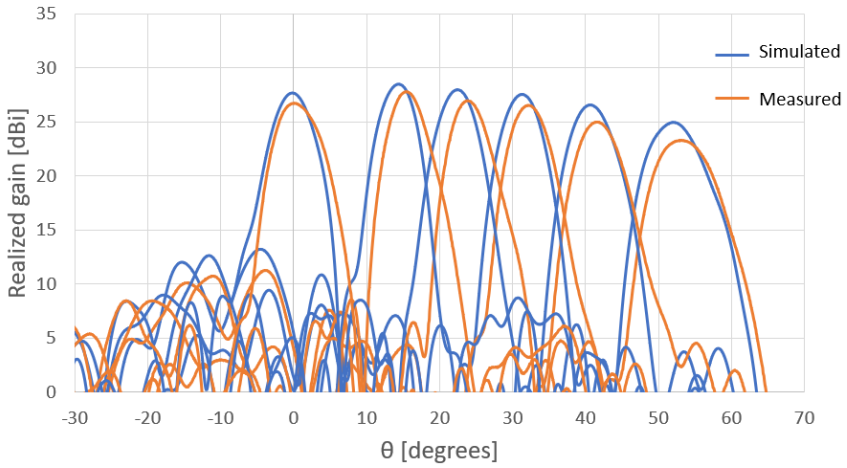

(a) 29.5 GHz

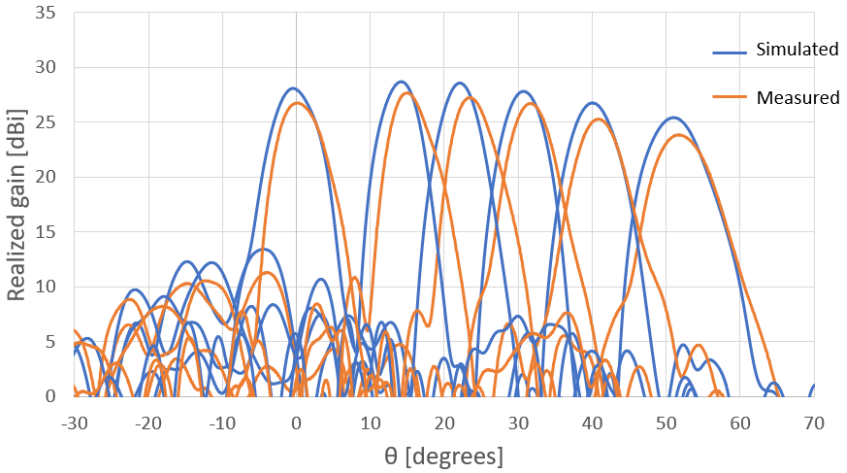

(b) 30.0 GHz

Figure 4.8: Simulated and measured farfield realized gain of the TA.

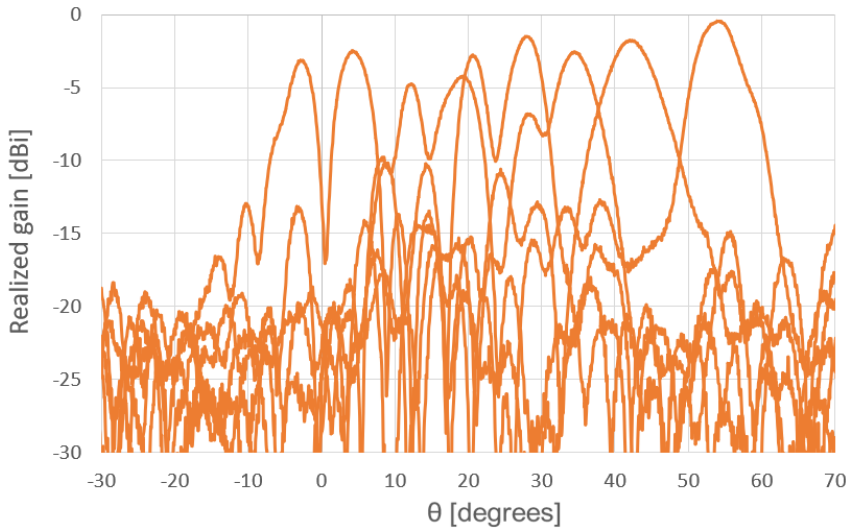

(a) 29.5 GHz

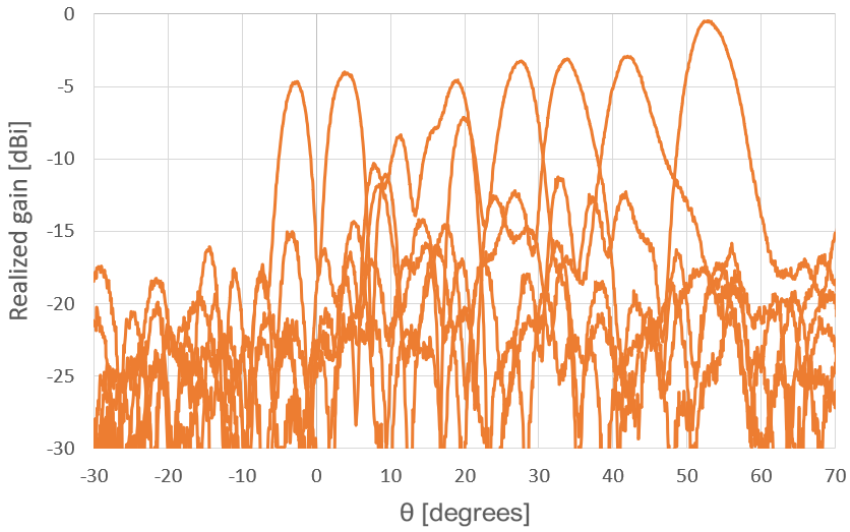

(b) 30.0 GHz

Figure 4.9: Measured cross component farfield realized gain of the TA.

5

Conclusion

Contents

5.1 Main Achievements

The objective of this thesis was the design and fabrication of a TA antenna working at the satellite uplink [29.5-30.0] GHz and capable of being 3D printed and provide beam steering up to 50 degrees. Its particularity was the use of a Gaussian beam as the source and formulation of the phase compensation for the design of the main lens, with the objective of eliminating or greatly reducing beam aberrations and SLL resulting from beam steering, compared to other solutions in the literature. The proposed solution was first analysed using a PO program and Mathematica and then designed, modeled and simulated using Mathematica and CST-MWS.

The chosen primary feed was obtained after designing and testing various lenses at different focal distances and dimensions such as to eliminate phase jumps and to obtain a thin lens and reduce beam deformity and reflections between this lens and the main one. The round lens has a radius of 67.5 mm and a minimum and maximum thickness of 0.3 mm and 4 mm respectively, and is at a focal distance of 80 mm from the horn antenna. It was possible to produce a Gaussian beam, the simulations of this feed show good agreement with the ideal Gaussian beam macro from CST-MWS, although the radiation pattern of this feed shows some distortion and a bump in the 0 degrees direction which lowers the directivity slightly. The prototype was fabricated in the Instituto de Telecomunicações (IT) facilities by 3D printing, as was the support structure for the two lenses, and the measurements showed good agreement with the simulations, for the [29.5-30.0] GHz band.

The TA lens was designed to compensate the phase of a Gaussian beam and have the fixed dimensions of 195 x 145 mm. It took several iterations to reach the final solution, experimenting with different cell dimensions, focal distances and lens positioning, as although the lens was designed for a focal distance F of 110 mm, it was positioned at a distance of 102.9 so the middle of the lens is at the 110 mm distance. The lens was also flipped. These adjustments were made because the radiation pattern showed an asymmetric main lobe in the central position, which was resolved. Some time was also dedicated to understanding the cause and attempting to eliminate the high radiation seen in the -20 to 0 degrees zone. It was concluded it was mostly due to the thickness of the lens, 14.2 mm at the thickest, as simulations with a higher permitivity and lower thickness greatly reduced this problem. In the end it was possible eliminate beam aberrations and lower SLL in the simulations in CST-MWS for a scanning range up to 51 degrees, although the scan loss was higher than seen in the literature. The prototype was also fabricated in the IT facilities by 3D printing and its measurements showed some aberrations but much lower than seen in the literature and otherwise showed good agreement with the simulations.

The overall antenna dimensions, including the support structure, were 195 x 175.4 mm and a height of 178.6 mm. At 30 GHz the simulated antenna has a maximum gain of 28.7 dBi, scan loss of 3.3 dB, scanning range of 51.4 degrees and SLL below -20 dB for all simulated feed displacements. The measured antenna has a maximum gain of 27.7 dBi, scan loss of 3.8 dB, scanning range of 51.6 degrees

and SLL below -19 dB measured feed displacements except for one, below -16 dB.

5.2 Future Work

It was proven that a Gaussian beam source TA reduces beam aberrations and SLL. This conclusion can be used as a starting point for a future work to improve scan loss, side lobe radiation in a non desired direction and overal antenna dimensions. As seen in Chapter 3, the main lens is quite thick due to the material used, and the cells have a high transmission loss. Other types of unit cells can be used to reduce the lens thickness and thus improve transmission loss and reduce the high radiation seen in the -20 to 0 degrees zone, such cells made of material with a higher permitivity or layered unit cells made from a combination of dielectric material and printed patches as seen in [3] or others, although most likely this would make fabrication more complex.

Antenna height is also not optimal and could be reduced using a more compact feed capable of producing a Gaussian beam.

Bibliography

[1] T. Hill, “Millimetre wave lens and transmitarray antennas for scan loss mitigation,” Ph.D. dissertation, 09 2019.

[2] “Gaussian beam.” [Online]. Available: https://www.techbriefs.com/component/content/article/tb/supplements/ptb/features/articles/12683#

[3] E. B. Lima, S. A. Matos, J. R. Costa, C. A. Fernandes, and N. J. Fonseca, “Circular Polarization Wide-Angle Beam Steering at Ka-Band by In-Plane Translation of a Plate Lens Antenna,” *IEEE Transactions on Antennas and Propagation*, 2015.

[4] “Gaussian beam.” [Online]. Available: https://commons.wikimedia.org/wiki/File:Gaussian_beam_with_german_description.svg

[5] ITU, “Evolving satellite communications,” *ITU News Magazine*, no. 2, p. 9, 2019. [Online]. Available: https://www.itu.int/en/myitu/Publications/2020/04/02/19/54/ITU-News-Magazine-No-2---2019

[6] S. Ye, X. Liang, W. Wang, R. Jin, J. Geng, T. S. Bird, and Y. J. Guo, “High-Gain planar antenna arrays for mobile satellite communications,” *IEEE Antennas and Propagation Magazine*, vol. 54, no. 6, pp. 256–268, 2012.

[7] M. Tripodi, F. Dimarca, T. Cadili, C. Mollura, F. Dimaggio, and M. Russo, “Ka band active phased array antenna system for satellite communication on the move terminal,” *Proceedings of the 5th European Conference on Antennas and Propagation, EUCAP 2011*, pp. 2628–2630, 2011.

[8] Y. A. Litinskaya, S. V. Polenga, A. V. Stankovsky, and Y. P. Salomatov, “A Ku-Band Low-Profile Wide-Angle Scanning Antenna Array with Combined Beam Steering,” *2018 14th International Scientific-Technical Conference on Actual Problems of Electronic Instrument Engineering, APEIE 2018 - Proceedings*, pp. 238–242, 2018.

[9] L. A. Greda and A. Dreher, “Tx-terminal phased array for satellite communication at Ka-band,” *Proceedings of the 37th European Microwave Conference, EUMC*, no. January, pp. 266–269, 2007.

[10] R. Vincenti Gatti, L. Marcaccioli, E. Sbarra, and R. Sorrentino, “Flat array antenna for Ku-band mobile satellite terminals,” *Proceedings of the 5th European Conference on Antennas and Propagation, EUCAP 2011*, pp. 2618–2622, 2011.

[11] W. M. Abdel-Wahab, H. Al-Saedi, M. Raeis-Zadeh, E. H. Mirza Alian, A. Ehsandar, G. Chen, A. Palizban, N. Ghafarian, H. El-Sawaf, M. R. Nezhad-Ahmadi, and S. Safavi Naeini, “Affordable Large Scale Active-Phased Array Antenna for Ka-Band Mobile SATCOM Applications,” *13th European Conference on Antennas and Propagation, EuCAP 2019*, vol. 1, no. EuCAP, pp. 1–4, 2019.

[12] P. Chen, W. Hong, H. Zhang, J. Chen, H. Tang, and Z. Chen, “Virtual Phase Shifter Array and Its Application on Ku Band Mobile Satellite Reception,” *IEEE Transactions on Antennas and Propagation*, vol. 63, no. 4, pp. 1408–1416, 2015.

[13] Y. Wang and A. M. Abbosh, “Software-defined reconfigurable antenna using slotted substrate integrated waveguide for Ka-band satellite-on-the-move communication,” *2015 International Symposium on Antennas and Propagation, ISAP 2015*, pp. 1–3, 2016.

[14] G. Wu, S. Qu, and S. Yang, “Wide-angle beam-scanning reflectarray with mechanical steering,” *IEEE Transactions on Antennas and Propagation*, vol. 66, no. 1, pp. 172–181, 2018.

[15] P. Naseri and S. V. Hum, “A Dual-Band Dual-Circularly Polarized Reflectarray for K / Ka-Band Space Applications,” *2019 13th European Conference on Antennas and Propagation (EuCAP)*, no. EuCAP, pp. 1–5, 2019.

[16] H. Bayer, A. Krauss, R. Stephan, and M. A. Hein, “A Dual-Band Multimode Monopulse Tracking Antenna for Land-Mobile Satellite Communications in Ka-Band,” no. March 2012, 2016.

[17] M. Li, M. A. Al-Joumayly, and N. Behdad, “Broadband true-time-delay microwave lenses based on miniaturized element frequency selective surfaces,” *IEEE Transactions on Antennas and Propagation*, vol. 61, no. 3, pp. 1166–1179, 2013.

[18] N. Gagnon and A. Petosa, “Using rotatable planar phase shifting surfaces to steer a high-gain beam,” *IEEE Transactions on Antennas and Propagation*, vol. 61, no. 6, pp. 3086–3092, 2013.

[19] N. Gagnon, A. Petosa, and D. A. Mcnamara, “Thin microwave quasi-transparent Phase-Shifting Surface (PSS),” *IEEE Transactions on Antennas and Propagation*, vol. 58, no. 4, pp. 1193–1201, 2010.

[20] H. Hasani, J. S. Silva, S. Capdevila, M. Garcia-Vigueras, and J. R. Mosig, “Dual-band circularly polarized transmitarray antenna for satellite communications at (20, 30) GHz,” *IEEE Transactions on Antennas and Propagation*, vol. 67, no. 8, pp. 5325–5333, 2019.

[21] L. W. Chen and Y. Ge, “A K-band flat transmitarray antenna with a planar microstrip slot-fed patch antenna feeder,” *Progress In Electromagnetics Research C*, vol. 64, no. March, pp. 97–104, 2016.

[22] P. Qin, L. Song, and Y. J. Guo, “Beam steering conformal transmitarray employing ultra-thin triple-layer slot elements,” *IEEE Transactions on Antennas and Propagation*, vol. 67, no. 8, pp. 5390–5398, 2019.

[23] H. Hasani, J. S. Silva, S. Capdevila, M. Garcia-Vigueras, and J. R. Mosig, “Dual-band circularly polarized transmitarray antenna for satellite communications at (20, 30) GHz,” *IEEE Transactions on Antennas and Propagation*, vol. 67, no. 8, pp. 5325–5333, 2019.

[24] A. Massaccesi, P. Pirinoli, V. Bertana, G. Scordo, S. L. Marasso, M. Cocuzza, and G. Dassano, “Broadband dielectric transmitarray with scanning capabilities,” in *2019 13th European Conference on Antennas and Propagation (EuCAP)*, 2019, pp. 1–2.

[25] N. Wang, B. Zhao, M. Fang, J. Qiu, and L. Xiao, “An element-staggered, wide-angle beam scanning transmitarray antenna with four focuses design,” in *2018 International Symposium on Antennas and Propagation (ISAP)*, 2018, pp. 1–2.

[26] L. Z. Song, P. Y. Qin, and Y. J. Guo, “Conformal transmitarray and its beam scanning,” in *2019 International Symposium on Antennas and Propagation (ISAP)*, 2019, pp. 1–3.

[27] U. N. Food and A. Ababa, “H Orn of a Frica – D Rought,” vol. 5, no. 3, pp. 1–5, 2011.

[28] L. Vinet and A. Zhedanov, “A ’missing’ family of classical orthogonal polynomials,” *Journal of Physics A: Mathematical and Theoretical*, vol. 44, no. 8, pp. 1689–1699, 2011.

[29] N. J. G. Fonseca, “Design and implementation of a closed cylindrical bfn-fed circular array antenna for multiple-beam coverage in azimuth,” *IEEE Transactions on Antennas and Propagation*, vol. 60, no. 2, pp. 863–869, 2012.

[30] B. Chantraine-Bares, R. Sauleau, L. Le Coq, and K. Mahdjoubi, “A new accurate design method for millimeter-wave homogeneous dielectric substrate lens antennas of arbitrary shape,” *IEEE Transactions on Antennas and Propagation*, vol. 53, no. 3, pp. 1069–1082, 2005.

[31] G. Godi, R. Sauleau, L. L. Coq, and D. Thouroude, “Design and optimization of three-dimensional integrated lens antennas with genetic algorithm,” *IEEE Transactions on Antennas and Propagation*, vol. 55, no. 3, pp. 770–775, 2007.

[32] C. Tian, Y. C. Jiao, G. Zhao, and H. Wang, “A Wideband Transmitarray Using Triple-Layer Elements Combined with Cross Slots and Double Square Rings,” *IEEE Antennas and Wireless Propagation Letters*, vol. 16, pp. 1561–1564, 2017.

[33] C. G. Ryan, M. R. Chaharmir, J. Shaker, J. R. Bray, Y. M. Antar, and A. Ittipiboon, "A wideband transmitarray using dual-resonant double square rings," *IEEE Transactions on Antennas and Propagation*, 2010.

[34] A. H. Abdelrahman, F. Yang, and A. Z. Elsherbeni, "Analysis of Multilayer Frequency Selective Surfaces for Transmitarray Antenna Applications," Tech. Rep.

[35] "Acrylonitrile Butadiene Styrene (ABS) Typical Properties Generic ABS." [Online]. Available: https://plastics.ulprospector.com/generics/1/c/t/acrylonitrile-butadiene-styrene-abs-properties-processing

[36] A.-e. Mahmoud, W. Hong, Y. Zhang, and A. Kishk, "W-Band Mutlilayer Perforated Dielectric Substrate Lens," vol. 13, pp. 734–737, 2014.

[37] K. T. Pham, R. Sauleau, E. Fourn, and A. Clemente, "Transmit-arrays at ka-band for harsh environment," in *2020 14th European Conference on Antennas and Propagation (EuCAP)*, 2020, pp. 1–4.

[38] X. Zhao, C. Yuan, L. Liu, S. Peng, Q. Zhang, and H. Zhou, "All-metal transmit-array for circular polarization design using rotated cross-slot elements for high-power microwave applications," *IEEE Transactions on Antennas and Propagation*, vol. 65, no. 6, pp. 3253–3256, 2017.

[39] S. H. Zainud-Deen, S. M. Gaber, and K. H. Awadalla, "Transmitarray using perforated dielectric material for wideband applications," *Progress In Electromagnetics Research M*, vol. 24, no. March, pp. 1–13, 2012.

[40] P. Naseri, S. A. Matos, J. R. Costa, and C. A. Fernandes, "Phase-delay versus phase-rotation cells for circular polarization transmit arrays—application to satellite ka-band beam steering," *IEEE Transactions on Antennas and Propagation*, vol. 66, no. 3, pp. 1236–1247, 2018.

[41] R. H. Phillion and M. Okoniewski, "Lenses for circular polarization using planar arrays of rotated passive elements," *IEEE Transactions on Antennas and Propagation*, vol. 59, no. 4, pp. 1217–1227, 2011.

[42] L. Di Palma, A. Clemente, L. Dussopt, R. Sauleau, P. Potier, and P. Pouliguen, "Circularly polarized transmitarray with sequential rotation in ka-band," *IEEE Transactions on Antennas and Propagation*, vol. 63, no. 11, pp. 5118–5124, 2015.

[43] "Wolfram Mathematica." [Online]. Available: http://www.wolfram.com/

[44] "CST - Computer Simulation Technology." [Online]. Available: https://www.cst.com/

[45] C. A. C. Fernandes, ""kh3d near. users manual, version 0.2h," instituto de telecomunicações - ist, feb 2018," Insituto de Telecomunicações - IST, Tech. Rep., 2018.